# Effect of boundary roughness on the attenuation of specular phonon reflection in graphene

Zhun-Yong Ong *

*Institute of High Performance Computing (IHPC), Agency for Science, Technology and Research (A*STAR), 1 Fusionopolis Way, #16-16 Connexis, Singapore 138632, Republic of Singapore*

(Received 26 January 2024; revised 27 March 2024; accepted 22 April 2024; published 20 May 2024)

The reduced phonon specularity $p$ from boundary roughness scattering plays a major role in the lower thermal conductivity in semiconducting and insulating nanowires and films. Although the well-known Ziman formula $p = \exp(-4\sigma^2 q_x^2)$, where $\sigma$ and $q_x$ denote the root-mean-square boundary roughness and the normal component of the incident phonon wave vector, respectively, and its variants are commonly used in the literature to estimate how roughness attenuates $p$, their validity and accuracy remain poorly understood, especially when the effects of mode conversion cannot be ignored. In this paper, we investigate the accuracy and validity of the more general Ogilvy formula, from which the Ziman formula is derived, by comparing its predictions to the $p$ values computed from atomistic Green's function simulations for an ensemble of rough boundaries in single-layer graphene. The effects of phonon dispersion, incident angle, polarization, mode conversion, and correlation length are analyzed. Our results suggest that the Ogilvy formula is remarkably accurate for $0 < q_x < \frac{\pi}{4\sigma}$ when the lateral correlation length $L$ is large or the phonon is at normal incidence. At large $q_x$ in the short-wavelength limit, the $q_x$-dependence of $p$ becomes significantly weaker. In the large-$L$ limit, the numerical results suggest the existence of a minimum $p$ for short-wavelength phonons, given by $p \sim p_0 \exp(-\pi^2/4)$, where $p_0$ is the baseline specularity for the ideal boundary.

DOI: 10.1103/PhysRevB.109.184207

## I. INTRODUCTION

The scattering of waves by rough boundaries, or *boundary roughness scattering* for short, is an area of long-standing interest in a wide range of fundamental and applied fields, such as optics [1], computer graphics [2], acoustics [3], nondestructive testing [4,5], seismology [6], and nanoscale thermal transport [7–11]. A problem of particular significance in boundary roughness scattering is the attenuated intensity of the specularly reflected wave, as characterized by the *specular reflectance*, which refers to the proportion of an incident wave that is scattered into the specular direction. For an ideal flat boundary, the incident wave is completely reflected in the specular direction because the *continuous* translational symmetry of the boundary requires the transverse component of the incident and reflected wave vectors in the plane of incidence (denoted by $\boldsymbol{q}_i$ and $\boldsymbol{q}_r$, respectively) to be conserved. This conservation condition is described by the generalized Snell's law, i.e., $q_i^{\parallel} = q_r^{\parallel}$, where the $\parallel$ superscript denotes the transverse component of the wave vector. For a nonideal boundary, the boundary roughness breaks this translational symmetry, resulting in the phenomenon of attenuated specular reflectance where the amplitude of the specularly reflected wave is reduced as part of the reflected wave is scattered in the nonspecular directions [12].

In condensed-matter physics, the phenomenon of boundary roughness scattering plays an important role in the reduced lattice thermal conductivity and thermoelectric properties of low-dimensional semiconductors (e.g., silicon nanowires and nanofilms). In these materials, thermal conduction in the bulk is primarily mediated by the propagation of phonons, the wavelike crystal lattice excitations that undergo scattering with the lattice boundary. In materials with rough boundaries [7,10,11,13], this boundary roughness scattering decreases the specular reflectance of the phonons and results in phonon momentum dissipation. For an incident wave or phonon, the degree of specular reflectance is characterized by the specularity parameter $p$, which represents the probability of specular reflection. When there is perfect specular reflection by an ideal boundary, we have $p = 1$ and no momentum dissipation in the axial direction of propagation. In the diffuse limit for an infinitely rough boundary, the incident phonon is assumed to be scattered equally in all directions such that $p = 0$. For a nonideal boundary of finite roughness, we expect $p$ to vary between 0 and 1, with the numerical value depending on the degree of boundary roughness, and this results in phonon momentum dissipation and resistance to thermal transport. In addition, the effective momentum exchange between the phonon and the boundary, which determines the impact of scattering on the thermal conductivity, also depends on the form of the diffuse field and the power spectrum of the boundary structure [13].

In spite of its relevance for understanding lattice thermal conduction, the boundary roughness scattering of phonons remains poorly characterized, especially in terms of the dependence of $p$ on the properties of the incident phonon (incident angle, polarization, and crystal momentum) and the structure of the boundary. For the benefit of the reader, we give a brief overview of the current theoretical description of

*ongzy@ihpc.a-star.edu.sg

 

the phenomenon. Current theories of how boundary roughness scattering attenuates $p$ rely heavily on analogies of scalar wave scattering by rough boundaries. In the simplest model, $p$ is related to the boundary roughness through the *Rayleigh formula* [14–16]

$$p = p_0 \exp(-4\Sigma^2), \tag{1}$$

where $\Sigma$ and $p_0$ denote the so-called Rayleigh roughness parameter [15] and the specularity parameter for the ideal boundary, respectively. In Eq. (1), we define $\Sigma$ as $\Sigma = \sigma q \cos\theta_i$, where $q$, $\sigma$, and $\theta_i$ denote the incident wave number, the root-mean-square (RMS) boundary roughness, and the angle of incidence, respectively. It should be noted that $p$ and $p_0$ are functions of $\theta_i$ and $q = \frac{2\pi}{\lambda}$, where $\lambda$ is the incident wavelength. Physically, Eq. (1) describes the exponential attenuation of the specularity parameter.

To be applicable, Eq. (1) must satisfy the Rayleigh roughness criterion, i.e., $\Sigma < \pi/4$ [15], which relates the boundary roughness to the incident wavelength, because the attenuation factor of $\exp(-4\Sigma^2)$ originates from the phase interference between random vertically aligned sites on the boundary. At larger values of $\sigma$ or shorter incident wavelengths (larger $q$'s), Eq. (1) is not expected to be valid when $q > \frac{\pi}{4\sigma}$ or $\lambda < 8\sigma$ although there is some uncertainty over the degree of its discrepancy with the actual $p$. In addition, Eq. (1) does not give an explicit dependence on the degree of undulation of the boundary, as characterized by its autocorrelation function $\langle h(\boldsymbol{r})h(0)\rangle$, where $h(\boldsymbol{r})$ is the displacement of the boundary from its mean position at the point $\boldsymbol{r}$, although Eq. (1) is derived from the *Kirchhoff approximation*, which assumes that the lateral correlation length $L$ is much greater than the wavelength, i.e., $qL \gg 1$ [8]. This means that Eq. (1) is also not valid at long wavelengths when $q \ll \frac{1}{L}$.

Taken together, the Rayleigh roughness criterion and the Kirchhoff approximation imply that the boundary roughness scattering for only a finite range of incident waves, as band-limited by the condition $\frac{1}{L} \ll q \lesssim \frac{\pi}{4\sigma}$, can be described by Eq. (1). A corollary of this is that Eq. (1) is not expected to be valid if $L \lesssim \sigma$. Equation (1) cannot describe the boundary scattering of long-wavelength waves unless the lateral correlation length is larger than the wavelength, and it also cannot describe the boundary scattering of short-wavelength waves unless the RMS boundary roughness is smaller than the wavelength. This is succinctly described by the condition

$$\sigma < \lambda \ll L. \tag{2}$$

In addition, it is common in the literature to ignore the angular dependence in Eq. (1) and simply set $p = \exp(-4\sigma^2 q^2)$, an expression that is sometimes attributed to Ziman [10,11] and significantly overestimates the phonon momentum dissipation from boundary roughness scattering, especially for phonons impinging on the boundary at a grazing angle [8].

In a crystal lattice, the wavelike phonons can similarly undergo scattering by boundary roughness, although two factors constrain the applicability of Eq. (1) for understanding how boundary roughness attenuates specular reflection. The first is the discrete lattice structure of the solid, which sets a minimum length scale absent from Eq. (1) and eliminates the continuous translational symmetry assumed in scalar wave models. The second is scattering-induced *mode conversion*, which changes the polarization of the incoming phonon. For example, an incoming longitudinal acoustic (LA) phonon can be scattered and transformed into an outgoing transverse acoustic (TA) phonon with a finite probability that depends on the angle of incidence. The additional effect of mode conversion means that the attenuation by boundary roughness is not a simple interference effect, as in the case of scalar wave scattering [15], but must account for the vectorial nature of the atomic displacement.

### A. The Ogilvy formula for phonons

Nevertheless, Eq. (1) lends itself to a possible generalization [14] that takes mode conversion into account. Let us associate each phonon with a polarization $\nu$ and wave vector $\boldsymbol{q}$ and use the subscripts $i$ and $r$ to label the incident and reflected phonons, respectively. We use the *mode-dependent* function $p_\sigma(\nu_r\boldsymbol{q}_r, \nu_i\boldsymbol{q}_i)$ to denote the transition probability that an incident $\nu_i\boldsymbol{q}_i$ phonon is *specularly* reflected into an outgoing $\nu_r\boldsymbol{q}_r$ phonon by a boundary of RMS roughness $\sigma$, and we can thus interpret $p_\sigma(\nu_r\boldsymbol{q}_r, \nu_i\boldsymbol{q}_i)$ intuitively as the ratio of the probability *flux* of the outgoing and incoming phonon modes given by $I^{\text{out}}(\nu_r\boldsymbol{q}_r)$ and $I^{\text{in}}(\nu_i\boldsymbol{q}_i)$, respectively. In other words, $p_\sigma(\nu_r\boldsymbol{q}_r, \nu_i\boldsymbol{q}_i) = I^{\text{out}}(\nu_r\boldsymbol{q}_r)/I^{\text{in}}(\nu_i\boldsymbol{q}_i)$. Physically, $I^{\text{in}}(\nu_i\boldsymbol{q}_i)$ describes the *incoming* flux of phonons with polarization $\nu_i$ (e.g., longitudinal acoustic) and wave vector $\boldsymbol{q}_i$. Likewise, $I^{\text{out}}(\nu_r\boldsymbol{q}_r)$ describes the *outgoing* flux of phonons with polarization $\nu_r$ and wave vector $\boldsymbol{q}_r$. The wave vectors $\boldsymbol{q}_i$ and $\boldsymbol{q}_r$ are not independent variables but are related through the generalized Snell's law ($q_i^{\parallel} = q_r^{\parallel}$) that expresses the conservation of transverse momentum.

Therefore, a natural generalization of Eq. (1) leads us to the expression [8]

$$p_\sigma(\nu_r\boldsymbol{q}_r, \nu_i\boldsymbol{q}_i) = p_0(\nu_r\boldsymbol{q}_r, \nu_i\boldsymbol{q}_i)\exp[-\sigma^2(|q_r^{\perp}| + |q_i^{\perp}|)^2], \tag{3}$$

where $p_0(\nu_r\boldsymbol{q}_r, \nu_i\boldsymbol{q}_i) = p_\sigma(\nu_r\boldsymbol{q}_r, \nu_i\boldsymbol{q}_i)|_{\sigma=0}$ denotes the specularity parameter for the ideal boundary, and the $\perp$ superscript on the right-hand side of Eq. (3) denotes the longitudinal component of the wave vector that is at normal incidence to the boundary. If there is no mode conversion ($\nu_r = \nu_i$), then $|q_r^{\perp}| = |q_i^{\perp}|$ and we recover the Rayleigh formula in Eq. (1). For the attenuation of elastodynamic waves by boundary roughness scattering, an analogous expression is given by Ogilvy in Ref. [14], which we refer to as the *Ogilvy formula* for convenience in the rest of this article. Because phonons in the long-wavelength limit are described by elastodynamic waves, we expect the Ogilvy formula to be applicable for the boundary roughness of phonons even though its validity and accuracy remain untested.

Nonetheless, our understanding of the accuracy of Eq. (3) for estimating the phonon specularity is poor, partly because of the challenges in the experimental measurement of individual phonon amplitudes [10,11,17]. Instead, the simpler Eq. (1), which ignores the effects of polarization, is more commonly used in the literature, especially for the interpretation of experimentally measured thermal conductivity values [10]. Even with the use of simulations [18], it is difficult to assess the accuracy of Eq. (3) because of the computational difficulties in isolating the specularly reflected wave

polarization components after the scattering. Furthermore, it is unclear how the nonlinear dispersion and discrete symmetries for phonons affect the validity of the Ogilvy formula, which is derived for elastodynamic waves in a continuum solid [14].

It is worth noting, however, that the results from an experimental study of the boundary scattering of phonons in silicon nanosheets [19] cast some doubt on the validity of Eqs. (1) and (3). In Ref. [19], the measured phonon specularity values are much smaller than those predicted using the Ziman theory, which is based on Eq. (1), with the geometrical boundary roughness of the silicon nanosheets used as the input. One possible explanation for the discrepancy is that Eq. (1) is not applicable to nanosheets, where the system has two opposite rough surfaces. Another is that Eqs. (1) and (3) are applicable but with the *effective* boundary roughness associated with scattering being much greater than the geometrical boundary roughness due to the changes in the morphology of the surfaces from amorphization or oxidation.

### B. Direct calculation of probability of specular reflection

However, the opportunity for assessing the accuracy of Eq. (3) has been greatly improved by extensions of the atomistic Green's function (AGF) method [20] for modeling mode-resolved phonon transmission and reflection [21,22] and recent advances in the identification of phonon polarization in lattice models [23]. These improved computational techniques allow us to efficiently identify the outgoing $\nu_r \boldsymbol{q}_r$ and the incoming $\nu_i \boldsymbol{q}_i$ phonon modes and hence calculate their scattering amplitude $S_\sigma(\nu_r \boldsymbol{q}_r, \nu_i \boldsymbol{q}_i)$, as defined in the equation

$$\psi^{\text{out}}(\nu_r \boldsymbol{q}_r) = S_\sigma(\nu_r \boldsymbol{q}_r, \nu_i \boldsymbol{q}_i)\psi^{\text{inc}}(\nu_i \boldsymbol{q}_i), \tag{4}$$

where $\psi^{\text{out}}$ and $\psi^{\text{inc}}$ are the *complex flux amplitudes* for the outgoing and incoming phonon modes, respectively, for the given lattice realization with the boundary roughness $\sigma$. Given that $S_\sigma(\nu_r \boldsymbol{q}_r, \nu_i \boldsymbol{q}_i)$ is a random variable, only ensemble averages of variables are meaningful. Thus, from Eq. (4), we obtain the exact expression for the probability of specular reflection, i.e.,

$$p_\sigma(\nu_r \boldsymbol{q}_r, \nu_i \boldsymbol{q}_i) = \langle |S_\sigma(\nu_r \boldsymbol{q}_r, \nu_i \boldsymbol{q}_i)_{q_r^\parallel = q_i^\parallel}|^2 \rangle, \tag{5}$$

where $\langle \cdots \rangle$ denotes the ensemble average of configurations with the same boundary configuration (roughness and correlation length), since $p_\sigma(\nu_r \boldsymbol{q}_r, \nu_i \boldsymbol{q}_i) = \langle I^{\text{out}}(\nu_r \boldsymbol{q}_r)/I^{\text{in}}(\nu_i \boldsymbol{q}_i) \rangle$ with $I^{\text{out}}(\nu_r \boldsymbol{q}_r) = |\psi^{\text{out}}(\nu_r \boldsymbol{q}_r)|^2$ and $I^{\text{in}}(\nu_r \boldsymbol{q}_r) = |\psi^{\text{in}}(\nu_r \boldsymbol{q}_r)|^2$. The subscript $q_r^\parallel = q_i^\parallel$ for $S_\sigma$ on the right-hand side of Eq. (5) indicates the conservation of transverse momentum in the scattering process. Therefore, using Eq. (5), we can test the validity of Eq. (3) because we can compute $p_\sigma$ and $p_0$ directly from the scattering amplitudes for a rough and flat boundary, respectively, with the AGF method.

### C. Scope and organization of the paper

In this paper, the aim and scope of our investigation are quite modest and specific. The primary object of our investigation is the extent of the validity of the Ogilvy formula from Eq. (3), which was originally derived for elastodynamic waves [14], for describing the *exponential attenuation* of the mode-dependent $p_\sigma$ from boundary roughness scattering in single-layer graphene (SLG). This is accomplished by computing the probability of specular reflection $p_\sigma$ in Eq. (5) directly with the extended AGF method. We investigate how the attenuation of $p_\sigma$ varies with respect to the properties of the boundary (e.g., roughness and correlation length) as well as the properties of the phonons (e.g., wave vector, polarization, and angle of incidence). It is hoped that our paper will shed light on some of the issues raised in earlier studies on boundary roughness scattering and provide complementary insights into existing work on phonon-boundary scattering [8,9,18,24]. By directly calculating $p_\sigma$ for a range of incident wave vectors $\boldsymbol{q}_i$, we circumvent some of the constraints (e.g., weak roughness, long wavelengths, linear dispersion and normal incidence) that arise from the approximations (e.g., the Kirchhoff approximation and the small-perturbation method) used in other work [8,9]. This allows us to probe the effects of boundary roughness scattering on $p_\sigma$ at grazing angles and short wavelengths comparable to or smaller than the RMS roughness. In particular, we address two issues that are not accessible in other methods or approximation but can be treated with the extended AGF method. The first one pertains to what happens to the attenuation of $p_\sigma$ at very small wavelengths. The second one is on how the attenuation differs when mode conversion takes place.

As our model of boundary roughness scattering in a condensed-matter system, we use a semi-infinite SLG lattice terminated by a stress-free boundary with in-plane roughness. We choose SLG as our model system for the following reasons. The first is that its two-dimensional (2D) lattice reduces the computational load of calculating the scattering amplitude as there is only one transverse dimension. The second is that its out-of-plane flexural acoustic (ZA) phonons, which have a quadratic dispersion ($\omega \propto k^2$) in the long-wavelength limit, allow us to study the effect of a nonlinear dispersion on Eq. (3). Also, because the boundary roughness is in-plane, the preservation of the symmetry in the out-of-plane direction means that there is no mode conversion between the flexural phonons and the in-plane phonons, simplifying our analysis of the applicability of Eq. (3) as mode conversion can only occur between the in-plane longitudinal acoustic (LA) and transverse acoustic (TA) phonons. Third, graphene has been promoted as a material for heat spreading in the thermal management of devices [25] because of its high native thermal conductivity. Thus, a clearer picture of boundary roughness scattering in graphene is highly desirable for understanding its thermal conductivity.

The organization of our paper is as follows. We discuss the statistical description of the boundary roughness in graphene, which we characterize using the topographic parameter $\mathcal{T}$. The method for generating the graphene boundary structure for a given RMS roughness $\sigma$ and lateral correlation length $L$ is described. We give an overview of the properties of the *bulk* acoustic phonons in graphene because the phonons are the wavelike excitations that undergo scattering. We then describe in some detail the AGF-based $S$-matrix method used in computing $p_\sigma$. For convenience in the characterization of the attenuation of $p_\sigma$, we introduce the mode-dependent *attenuation parameter* $\chi$ which is related to the Rayleigh roughness parameter $\Sigma$. The dependence of $p_\sigma$ and $\chi$, which we compute

from our simulation results, on the boundary structure and bulk acoustic phonon properties is discussed. In particular, we pay attention to the areas where $\chi$ agrees and disagrees with the predictions of the Ogilvy formula, and we characterize the behavior of $\chi$ when the Ogilvy formula is not expected to be valid (e.g., short wavelengths). We also measure the effective boundary roughness $\rho_{\text{fit}}$, which we determine from fitting the attenuation of $p_\sigma$, and we compare it to the geometrical RMS roughness $\sigma$ of the structure.

## II. GRAPHENE BOUNDARY SCATTERING

### A. Atomistic model of rough graphene boundary

#### 1. Statistical characterization of boundary roughness

In our setup, the semi-infinite SLG sheet, which extends indefinitely to the left ($x < 0$), is located on the $x$-$y$ plane and terminated by a boundary with its mean position ($x = 0$) parallel to the $y$ axis. Thus, the longitudinal and transverse directions are parallel to the $x$ and $y$ axis, respectively. Along the $x = 0$ line, the edge of the rough boundary is statistically characterized by the *continuous* random displacement function $h(y)$ which satisfies the Gaussian correlation function [8],

$$\langle h(y)h(0)\rangle = \sigma^2 \exp(-y^2/L^2), \tag{6}$$

where $\sigma = \sqrt{\langle h\rangle^2}$ and $L$ denote the RMS roughness and the lateral correlation length along the $y$ axis, respectively. We also define the mean displacement $\overline{h(y)}$ to be zero. The boundary is characterized by two length-scale parameters: $R_0 = 2\sqrt{3}a_{\text{cc}}$ for the RMS roughness and $L_0 = 3a_{\text{cc}}$ for the correlation length, where $a_{\text{cc}}$ is the equilibrium carbon-carbon (C-C) bond length in bulk graphene. The correlation length $L$ along the $y$ axis can be interpreted as the characteristic *feature size* of the boundary. When $L$ is small (large), the boundary has a greater (smaller) lineal density of peaks and valleys.

To characterize the statistical topography, or loosely speaking, the degree of jaggedness of the boundary, we also define and use the dimensionless parameter $\mathcal{T} \equiv \sigma/L$, which we will refer to as the *topographic parameter* in the rest of the article. When $\mathcal{T}$ is large (small), the boundary is more (less) jagged. In general for the boundary roughness scattering of a scalar wave, the Rayleigh roughness criterion and the Kirchhoff approximation taken together imply that the Ogilvy formula in Eq. (3) is only valid when $\mathcal{T} \lesssim 1$ in addition to the condition in Eq. (2). We hypothesize that this is also true for the boundary roughness scattering of phonons in a graphene lattice and that the accuracy of the Ogilvy formula increases as $\mathcal{T}$ decreases (i.e., less jagged).

#### 2. Atomistic realization of the rough graphene boundary

For a graphene lattice, the orientation can be classified as either "zigzag-edge" or "armchair-edge" to describe the translational symmetry of the lattice in the $y$ direction. In a zigzag-edge graphene lattice, the arrangement of the C-C bonds in the $y$ direction has a zigzag-like pattern. Likewise, in an armchair-edge graphene lattice, the arrangement is armchair-like. In our paper, we limit the scope of our investigation to the boundaries of zigzag-edge graphene for convenience as the periodicity of the zigzag-edge boundary in the $y$ direction is smaller and thus closer to a smooth boundary.

Although Eq. (6) describes the structure of a continuous boundary, it is not immediately applicable to the graphene lattice, which is discrete and has a minimum length scale associated with $a_{\text{cc}}$. Thus, it is necessary to introduce a procedure that maps the continuous boundary described by $h(y)$ to the positions of the boundary C atoms. In our simulations, to construct the atomistic realization of the boundary described by an instance of $h(y)$, we first divide the graphene lattice into hexagonal subunits with each subunit centered at $(x_{\text{c}}, y_{\text{c}})$ and consisting of six C atoms. If the $x_{\text{c}}$ of a hexagonal subunit is positioned to the left of the continuous boundary such that $x_{\text{c}} < h(y_{\text{c}})$, then its six atoms are incorporated into the simulated boundary structure. This procedure ensures that there are no dangling C-C bonds at the boundary, i.e., each boundary atom is connected to at least two other atoms. Figure 1 shows the realization of a rough boundary of zigzag-edge graphene corresponding to an instance of $h(y)$. After the positions of the C atoms are set, the entire structure is optimized in GULP [26] using the REBO potential [27]. We obtain a value of $a_{\text{cc}} = 1.4203$ Å from the optimization of bulk graphene. Although the REBO potential has not been optimized for the phonon dispersion of graphene [28], we use it because it can accommodate a sufficiently large and stable rough boundary needed for both the zigzag and armchair-edge boundary and the primary objective of our work is to understand the effect of boundary roughness on specularity at an atomistic level.

In our simulations, the width (lineal cross-section) of the zigzag-edge boundary and layers is $W = 275.56$ Å in the $y$ direction. This is the largest $W$ value that we can use in GULP to extract the IFC values. We impose periodic boundary conditions for $h(y)$ in the $y$ direction so that $h(0) = h(W)$. For each combination of $L$ and $\sigma$, we generate 20 instances of $h(y)$, which we need for computing ensemble-averaged quantities $\langle\cdots\rangle$ in Eq. (5), and we use each one to construct an atomistic model of the boundary for the zigzag-edge graphene lattice. For each atomistic boundary model, we calculate the interatomic force-constant (IFC) matrices $\boldsymbol{H}_{\text{B}}$ and $\boldsymbol{H}_{\text{LB}}$ that describe the mass-normalized harmonic forces within the boundary region (Fig. 1) and the harmonic forces between the bulk and the boundary region.

Figure 2(a) shows the phonon dispersion curves for graphene, with each phonon branch distinctly color-coded, using the interatomic force constants generated in GULP after the structure for bulk graphene is optimized. The identification and labeling of the phonon branch or polarization for each eigenmode is carried out by using the method described in Ref. [23]. In our work, we ignore the optical phonons and limit the scope in our study of boundary roughness scattering to the acoustic phonons, which have three distinct branches in graphene, because the Ogilvy formula from Eq. (3) is only applicable to the acoustic waves. Figures 2(b)–2(d) show the two-dimensional distribution of the eigenmode frequency $\omega$ over the first Brillouin zone as a function of the wave vector $\boldsymbol{q}$, which we compute using the REBO potential, for the flexural acoustic (ZA), transverse acoustic (TA), and longitudinal acoustic (LA) phonons. In the long-wavelength limit near the $\Gamma$ point, the LA and TA branches exhibit a linear dispersion ($\omega \propto q$) and have a well-defined wave speed, while the ZA

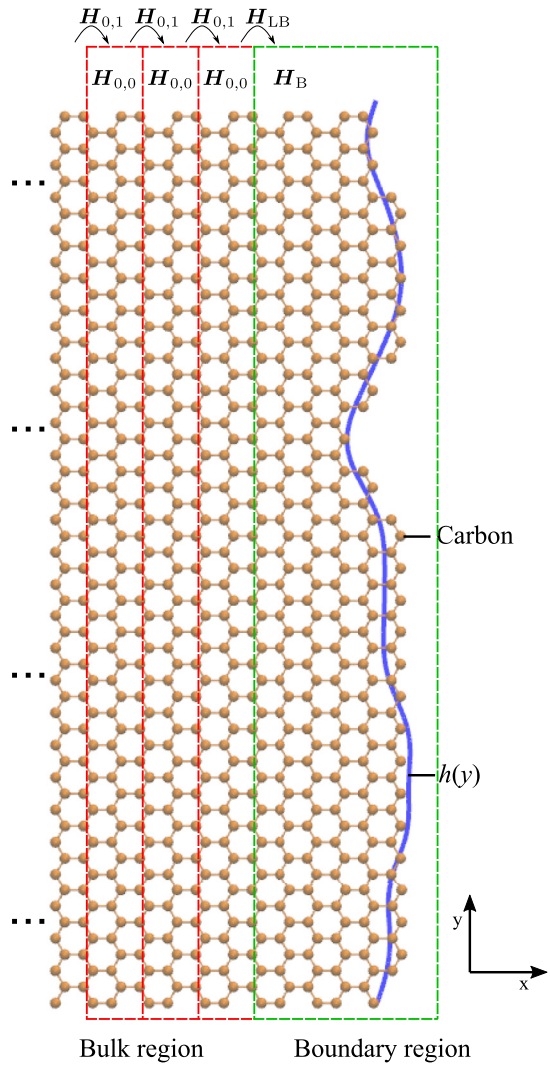


FIG. 1. We plot of a realization of $h(y)$, indicated by the blue solid line, and superimpose it on the corresponding lattice structure of the zigzag-edge boundary of graphene for $\sigma = 0.5R_0$ and $L = L_0$. We impose periodic boundary conditions in the $y$ direction. The lattice extends indefinitely to the left while it is terminated by a rough boundary on the right. The boundary and bulk regions are bounded by green and red dashed lines, respectively.

branch has a quadratic dispersion ($\omega \propto q^2$). The slope for the LA phonon branch is also significantly greater than the slope for the TA phonon branch, with the average longitudinal wave speed $c_L$ (19.6 km/s) nearly twice the average transverse wave speed $c_T$ (10.7 km/s), the values of which we extract from Fig. 2(a).

### B. Methodology for *S* matrix calculation

To describe the elastic scattering of phonons, we adopt the extended AGF method [29,30] which is developed in Refs. [21,22] to describe mode-resolved transmission and reflection, and it has been used to characterize diffuse phonon scattering by graphene grain boundaries [31,32]. The reader may skip this part of the paper and proceed directly to Sec. III as the details of the calculation given in Secs. II B 1–II B 3 are not necessary for understanding the results discussed in Sec. III, although we give an overview of the AGF method here. The inputs for the extended AGF method are the mass-normalized IFC submatrices ($\boldsymbol{H}_{0,0}$ and $\boldsymbol{H}_{0,1}$) associated with the bulk and the boundary region ($\boldsymbol{H}_B$ and $\boldsymbol{H}_{LB}$) as shown in Fig. 1. For each boundary structure, we use these four input submatrices to compute the frequency-dependent $S$ matrix for each $\omega$ over the frequency range from $\omega = 0.5 \times 10^{13}$ to $2.2 \times 10^{14}$ rad/s at intervals of $\Delta\omega = 0.5 \times 10^{13}$ rad/s, with the upper bound of this range limited by the highest possible LA phonon frequency at the $K$ point in Fig. 2(a).

At each $\omega$ step, all the possible incoming phonon modes are computed in the AGF method, with the polarization and wave vector of each mode labeled $\nu_i \boldsymbol{q}_i$. All of the possible outgoing modes are also similarly computed, with each labeled $\nu_r \boldsymbol{q}_r$. We then extract the target matrix elements $S_\sigma(\nu_r \boldsymbol{q}_r, \nu_i \boldsymbol{q}_i)_{q_r^\parallel = q_i^\parallel}$ for the ensemble of boundary structures corresponding to a $\sigma, L$ combination, and we compute the specularity parameter or probability of specular reflection $p_\sigma(\nu_r \boldsymbol{q}_r, \nu_i \boldsymbol{q}_i)$ as given in Eq. (5). The key formulas for computing the $S$ matrix are given in Eqs. (9)–(17).

#### 1. *Extraction of input submatrices in bulk and boundary structure*

In the bulk graphene lattice, the atoms can be arranged as a periodic array of layers in the direction perpendicular to the boundary so that the overall IFC matrix can be expressed in the block-tridiagonal form

$$\mathbf{H}_{\text{bulk}} = \begin{pmatrix} \ddots & \ddots & & & \\ \ddots & \boldsymbol{H}_{-1,-1} & \boldsymbol{H}_{-1,0} & & \\ & \boldsymbol{H}_{-1,0}^\dagger & \boldsymbol{H}_{0,0} & \boldsymbol{H}_{0,1} & \\ & & \boldsymbol{H}_{0,1}^\dagger & \boldsymbol{H}_{1,1} & \ddots \\ & & & \ddots & \ddots \end{pmatrix}, \tag{7}$$

where the submatrix $\boldsymbol{H}_{m,n}$ represents the mass-normalized IFC coupling of layer $n$ to layer $m$ and $\boldsymbol{H}_{m,n}^\dagger = \boldsymbol{H}_{n,m}$. The short-range interatomic forces imply that only neighboring layers are coupled, i.e., only the submatrices $\boldsymbol{H}_{n,n-1}$, $\boldsymbol{H}_{n,n}$, and $\boldsymbol{H}_{n,n+1}$ have nonzero matrix elements. The translational symmetry means that each layer is identical so that $\boldsymbol{H}_{0,0} = \boldsymbol{H}_{1,1} = \cdots$ and $\boldsymbol{H}_{-1,0} = \boldsymbol{H}_{0,1} = \cdots$. Hence, only two unique submatrices $\boldsymbol{H}_{0,0}$ and $\boldsymbol{H}_{0,1}$ are needed to construct $\mathbf{H}_{\text{bulk}}$. The IFC matrix for the semi-infinite graphene system with a rough boundary has the form

$$\mathbf{H}_{\text{boundary}} = \begin{pmatrix} \ddots & \ddots & & & \\ \ddots & \boldsymbol{H}_{0,0} & \boldsymbol{H}_{0,1} & & \\ & \boldsymbol{H}_{0,1}^\dagger & \boldsymbol{H}_{0,0} & \boldsymbol{H}_{0,1} & \\ & & \boldsymbol{H}_{0,1}^\dagger & \boldsymbol{H}_{0,0} & \boldsymbol{H}_{LB} \\ & & & \boldsymbol{H}_{LB}^\dagger & \boldsymbol{H}_B \end{pmatrix}, \tag{8}$$

where $\boldsymbol{H}_B$ describes the IFC coupling within the boundary region shown in Fig. 1 while $\boldsymbol{H}_{LB}$ describes the IFC coupling between the bulk and the boundary region. The correspondence of the individual IFC submatrices ($\boldsymbol{H}_{0,0}, \boldsymbol{H}_{0,1}, \boldsymbol{H}_{LB}$, and $\boldsymbol{H}_B$) to the arrangement of the layers in the simulated system

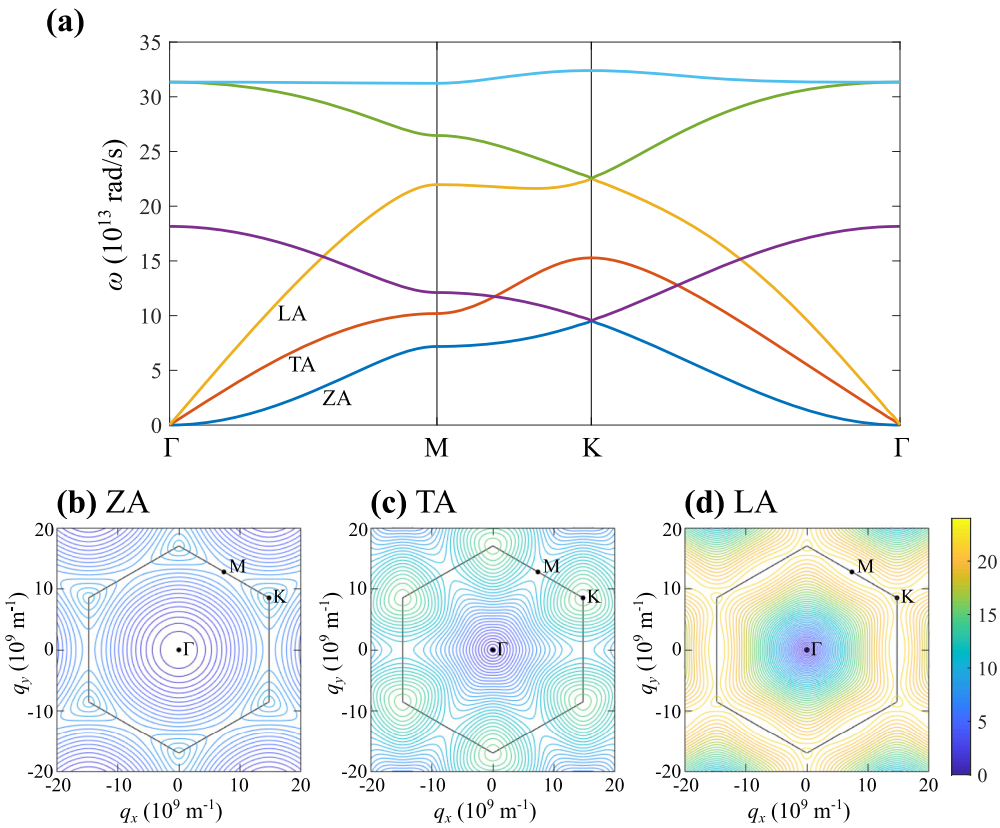


FIG. 2. (a) Plot of the bulk phonon dispersion between the symmetry points (Γ, $K$, and $M$) in the Brillouin zone of zigzag-edge graphene. The dispersion curves are calculated using the IFC matrices obtained with the REBO potential. The different acoustic phonon branches are identified using the method in Ref. [23] and colored according to their polarization. In the long-wavelength limit near the Γ point, the LA and TA branches exhibit a linear dispersion ($\omega \propto q$) while the ZA branch has a quadratic dispersion ($\omega \propto q^2$). Panels (b)–(d) show the two-dimensional contour plots of the dispersion in reciprocal space for the ZA, TA and LA phonons in zigzag-edge graphene with $\omega$ indicated in color. The Brillouin zone boundary is indicated by the solid gray lines. The frequency contours are drawn in intervals of $\Delta\omega = 0.5 \times 10^{13}$ rad/s.

is shown in Fig. 1. We extract the first pair of submatrices $\boldsymbol{H}_{0,0}$ and $\boldsymbol{H}_{0,1}$ from $\mathbf{H}_{\text{bulk}}$ and the second pair $\boldsymbol{H}_{\text{LB}}$ and $\boldsymbol{H}_{\text{B}}$ from $\mathbf{H}_{\text{boundary}}$.

### 2. *Computation of Bloch matrices and eigenmodes associated with bulk graphene*

To study the elastic scattering of phonons, we limit the dynamics to a fixed frequency $\omega$. At each frequency $\omega$, to find the eigenmodes associated with the translational symmetry of the bulk region in the longitudinal $x$ direction, we need to use the submatrices $\boldsymbol{H}_{0,0}$ and $\boldsymbol{H}_{0,1}$ from Sec. II B 1. We first define the frequency-dependent surface Green's function matrices $\boldsymbol{g}^{\text{ret}}_{\text{L},-}(\omega)$ and $\boldsymbol{g}^{\text{adv}}_{\text{L},-}(\omega)$:

$$\boldsymbol{g}^{\text{ret}}_{\text{L},-}(\omega) = \left[(\omega + i0^+)^2\boldsymbol{I} - \boldsymbol{H}_{0,0} - \boldsymbol{H}^\dagger_{0,1}\boldsymbol{g}^{\text{ret}}_{\text{L},-}\boldsymbol{H}_{0,1}\right]^{-1}, \quad (9a)$$

$$\boldsymbol{g}^{\text{adv}}_{\text{L},-}(\omega) = \boldsymbol{g}^{\text{ret}}_{\text{L},-}(\omega)^\dagger. \quad (9b)$$

Given Eq. (9), we define the *Bloch matrices* $\boldsymbol{F}^{\text{ret}}_{\text{L},-}(\omega)$ and $\boldsymbol{F}^{\text{adv}}_{\text{L},-}(\omega)$:

$$\left[\boldsymbol{F}^{\text{ret}}_{\text{L},-}(\omega)\right]^{-1} = \boldsymbol{g}^{\text{ret}}_{\text{L},-}(\omega)\boldsymbol{H}_{0,1}, \quad (10a)$$

$$\left[\boldsymbol{F}^{\text{adv}}_{\text{L},-}(\omega)\right]^{-1} = \boldsymbol{g}^{\text{adv}}_{\text{L},-}(\omega)\boldsymbol{H}_{0,1}, \quad (10b)$$

which describe the translational symmetry of the eigenmodes. This allows us to determine the Bloch eigenmode matrices $\boldsymbol{U}^{\text{ret}}_{\text{L},-}(\omega)$ and $\boldsymbol{U}^{\text{adv}}_{\text{L},-}(\omega)$:

$$\left[\boldsymbol{F}^{\text{ret}}_{\text{L},-}(\omega)\right]^{-1}\boldsymbol{U}^{\text{ret}}_{\text{L},-}(\omega) = \boldsymbol{U}^{\text{ret}}_{\text{L},-}(\omega)\left[\boldsymbol{\Lambda}^{\text{ret}}_{\text{L},-}(\omega)\right]^{-1}, \quad (11a)$$

$$[\boldsymbol{F}^{\text{adv}}_{\text{L},-}(\omega)]^{-1}\boldsymbol{U}^{\text{adv}}_{\text{L},-}(\omega) = \boldsymbol{U}^{\text{adv}}_{\text{L},-}(\omega)\left[\boldsymbol{\Lambda}^{\text{adv}}_{\text{L},-}(\omega)\right]^{-1}, \quad (11b)$$

associated with the outgoing leftward-propagating ($\boldsymbol{U}^{\text{ret}}_{\text{L},-}$) and incoming rightward-propagating ($\boldsymbol{U}^{\text{adv}}_{\text{L},-}$) phonon eigenmodes at frequency $\omega$. The eigenvalue matrices $\boldsymbol{\Lambda}^{\text{ret}}_{\text{L},-}(\omega)$ and $\boldsymbol{\Lambda}^{\text{adv}}_{\text{L},-}(\omega)$ have the diagonal form

$$\boldsymbol{\Lambda}^{\text{ret}}_{\text{L},-}(\omega) = \begin{pmatrix} e^{ik_1^\perp a} & & \\ & e^{ik_2^\perp a} & \\ & & \ddots \end{pmatrix},$$

where $k_1^\perp, k_2^\perp, \ldots$ are the "folded" wave-vector components in the longitudinal $x$ direction for the phonon eigenmodes at frequency $\omega$. Because of the periodic boundary condition in the transverse ($y$) direction, we can also associate each phonon eigenmode with a "folded" wave-vector component in the transverse direction and determine the corresponding set of transverse wave vectors $k_1^\parallel, k_2^\parallel, \ldots$ . Using the zone-unfolding

method from Ref. [22], we can map each of the "folded" 2D wave vectors, e.g., $\boldsymbol{k} = (k^{\perp}, k^{\parallel})$, to an unfolded 2D wave vector $\boldsymbol{q} = (q_x, q_y)$ corresponding to a unique wave vector within the first Brillouin zone. Therefore, we can associate each phonon eigenmode with an unfolded wave vector, and thus the phonon eigenmode matrix from Eq. (11) can be expressed as

$$\boldsymbol{U}^{\text{ret}}_{\text{L},-}(\omega) = \left[\boldsymbol{u}^{\text{ret}}_{\text{L},-}(\boldsymbol{q}_1), \boldsymbol{u}^{\text{ret}}_{\text{L},-}(\boldsymbol{q}_2), \ldots\right], \tag{12a}$$

where $\boldsymbol{u}^{\text{ret}}_{\text{L},-}(\boldsymbol{q})$ is the column vector corresponding to the outgoing phonon eigenmode with wave vector $\boldsymbol{q}$, which is real for bulk phonon modes and complex for evanescent modes, at frequency $\omega$. In addition, a unique phonon polarization $\nu$ can be associated with the phonon eigenmode for $\boldsymbol{q}$ and $\omega$, using the method described in Ref. [23]. Similarly, we can write

$$\boldsymbol{U}^{\text{adv}}_{\text{L},-}(\omega) = \left[\boldsymbol{u}^{\text{adv}}_{\text{L},-}(\boldsymbol{q}'_1), \boldsymbol{u}^{\text{adv}}_{\text{L},-}(\boldsymbol{q}'_2), \ldots\right], \tag{12b}$$

where $\boldsymbol{u}^{\text{adv}}_{\text{L},-}(\boldsymbol{q}')$ is the column vector corresponding to the incoming phonon eigenmode with wave vector $\boldsymbol{q}'$.

Given the Bloch eigenmodes from Eq. (12), we also define their associated eigenvelocity matrices $\boldsymbol{V}^{\text{ret}}_{\text{L},-}(\omega)$ and $\boldsymbol{V}^{\text{adv}}_{\text{L},-}(\omega)$:

$$\boldsymbol{V}^{\text{ret}}_{\text{L},-}(\omega) = -\frac{ia_{\text{L}}}{2\omega}\left(\boldsymbol{U}^{\text{ret}}_{\text{L},-}\right)^{\dagger}\boldsymbol{H}^{\dagger}_{0,1}\left[\boldsymbol{g}^{\text{ret}}_{\text{L},-} - \left(\boldsymbol{g}^{\text{ret}}_{\text{L},-}\right)^{\dagger}\right]\boldsymbol{H}_{0,1}\boldsymbol{U}^{\text{ret}}_{\text{L},-}, \tag{13a}$$

$$\boldsymbol{V}^{\text{adv}}_{\text{L},-}(\omega) = -\frac{ia_{\text{L}}}{2\omega}\left(\boldsymbol{U}^{\text{adv}}_{\text{L},-}\right)^{\dagger}\boldsymbol{H}^{\dagger}_{0,1}\left[\boldsymbol{g}^{\text{adv}}_{\text{L},-} - \left(\boldsymbol{g}^{\text{adv}}_{\text{L},-}\right)^{\dagger}\right]\boldsymbol{H}_{0,1}\boldsymbol{U}^{\text{adv}}_{\text{L},-}, \tag{13b}$$

where $a_{\text{L}}$ is the interlayer distance. The eigenvelocity matrices from Eq. (13) have the diagonal form

$$\boldsymbol{V}^{\text{ret}}_{\text{L},-}(\omega) = \begin{pmatrix} v^{\text{ret}}_{\text{L},-}(\boldsymbol{q}_1) & & \\ & v^{\text{ret}}_{\text{L},-}(\boldsymbol{q}_2) & \\ & & \ddots \end{pmatrix},$$

$$\boldsymbol{V}^{\text{adv}}_{\text{L},-}(\omega) = \begin{pmatrix} v^{\text{adv}}_{\text{L},-}(\boldsymbol{q}'_1) & & \\ & v^{\text{adv}}_{\text{L},-}(\boldsymbol{q}'_2) & \\ & & \ddots \end{pmatrix},$$

where $v^{\text{ret}}_{\text{L},-}(\boldsymbol{q})$ and $v^{\text{adv}}_{\text{L},-}(\boldsymbol{q})$ are the longitudinal velocity components for the outgoing and incoming phonon modes with wave vector $\boldsymbol{q}$, respectively. Because the incoming phonon modes are traveling rightward towards the boundary while the outgoing phonon modes are traveling leftward away from the boundary, we have $v^{\text{ret}}_{\text{L},-} \leqslant 0$ and $v^{\text{adv}}_{\text{L},-} \geqslant 0$.

#### *3. Computation of reflection matrix and scattering amplitudes*

Finally, to compute the scattering amplitudes of the reflected phonons, we need the Green's function submatrix for the boundary region in the semi-infinite SLG sheet,

$$\boldsymbol{G}^{\text{ret}}_{\text{B}}(\omega) = \left[(\omega + i0^{+})^2\boldsymbol{I}_{\text{B}} - \boldsymbol{H}_{\text{B}} - \boldsymbol{H}^{\dagger}_{\text{LB}}\boldsymbol{g}^{\text{ret}}_{\text{L},-}\boldsymbol{H}_{\text{LB}}\right]^{-1}, \tag{14}$$

which requires all four input submatrices ($\boldsymbol{H}_{0,0}$, $\boldsymbol{H}_{0,1}$, $\boldsymbol{H}_{\text{LB}}$, and $\boldsymbol{H}_{\text{B}}$). We also define

$$\boldsymbol{Q}_{\text{L}}(\omega) = (\omega + i0^{+})^2\boldsymbol{I} - \boldsymbol{H}_{0,0} - \boldsymbol{H}^{\dagger}_{0,1}\boldsymbol{g}^{\text{ret}}_{\text{L},-}\boldsymbol{H}_{0,1} - \boldsymbol{H}_{0,1}\boldsymbol{g}^{\text{ret}}_{\text{L},+}\boldsymbol{H}^{\dagger}_{0,1}, \tag{15}$$

where $\boldsymbol{g}^{\text{ret}}_{\text{L},+}(\omega) = [(\omega + i0^{+})^2\boldsymbol{I} - \boldsymbol{H}_{0,0} - \boldsymbol{H}_{0,1}\boldsymbol{g}^{\text{ret}}_{\text{L},+}(\omega)\boldsymbol{H}^{\dagger}_{0,1}]^{-1}$.

Given Eqs. (14) and (15), the reflection matrix, which relates the amplitude of the outgoing phonon flux to the incoming phonon flux, is given by

$$\boldsymbol{r}_{\text{LL}}(\omega) = \frac{2i\omega}{a_{\text{L}}}\left(\boldsymbol{V}^{\text{ret}}_{\text{L},-}\right)^{1/2}\left(\boldsymbol{U}^{\text{ret}}_{\text{L},-}\right)^{-1}\left(\boldsymbol{G}^{\text{ret}}_{\text{L}} - \boldsymbol{Q}^{-1}_{\text{L}}\right) \times \left(\boldsymbol{U}^{\text{adv}\,\dagger}_{\text{L},-}\right)^{-1}\left(\boldsymbol{V}^{\text{adv}}_{\text{L},-}\right)^{1/2}, \tag{16}$$

where $\boldsymbol{G}^{\text{ret}}_{\text{L}}(\omega) = \boldsymbol{g}^{\text{ret}}_{\text{L},-} + \boldsymbol{g}^{\text{ret}}_{\text{L},-}\boldsymbol{H}_{\text{LB}}\boldsymbol{G}^{\text{ret}}_{\text{B}}\boldsymbol{H}^{\dagger}_{\text{LB}}\boldsymbol{g}^{\text{ret}}_{\text{L},-}$. We obtain the reduced reflection matrix $\bar{\boldsymbol{r}}_{\text{LL}}$ from Eq. (16) by eliminating the matrix columns and rows associated with the evanescent modes. The matrix $\bar{\boldsymbol{r}}_{\text{LL}}$ is an $N \times N$ matrix of the form

$$\bar{\boldsymbol{r}}_{\text{LL}} = \begin{pmatrix} S(\nu_1\boldsymbol{q}_1, \nu'_1\boldsymbol{q}'_1) & \cdots & S(\nu_1\boldsymbol{q}_1, \nu'_N\boldsymbol{q}'_N) \\ \vdots & \ddots & \vdots \\ S(\nu_N\boldsymbol{q}_N, \nu'_1\boldsymbol{q}'_1) & \cdots & S(\nu_N\boldsymbol{q}_N, \nu'_N\boldsymbol{q}'_N) \end{pmatrix}, \tag{17}$$

where $S(\nu_n\boldsymbol{q}_n, \nu'_m\boldsymbol{q}'_m)$ is the complex scattering amplitude between the incoming $\nu'_m\boldsymbol{q}'_m$ phonon mode and the outgoing $\nu_n\boldsymbol{q}_n$ phonon mode from Eq. (12). We note here that because the width of the system $W$ is finite, the transverse components of the wave vectors for the incoming and outgoing modes, $q_i^{\parallel}$ and $q_r^{\parallel}$, are discretized such that $q^{\parallel} = \frac{2\pi n}{W}$, where $n$ in an integer. To compute the specularity parameter $p_\sigma(\nu_r\boldsymbol{q}_r, \nu_i\boldsymbol{q}_i)$ from Eq. (5), we take $\nu_r$, $\nu_i$, and $\boldsymbol{q}_i$ as inputs and find the matching matrix element $S(\nu_r\boldsymbol{q}_r, \nu_i\boldsymbol{q}_i)$ from Eq. (17) for which $q_r^{\parallel} = q_i^{\parallel}$ to obtain $S_\sigma(\nu_r\boldsymbol{q}_r, \nu_i\boldsymbol{q}_i)_{q_r^{\parallel}=q_i^{\parallel}}$ for that particular boundary.

## III. SIMULATION RESULTS AND DISCUSSION

### A. Attenuation parameter $\chi$

We can quantify the attenuation of the specular reflection by using the ratio

$$\zeta_\sigma(\nu_r\boldsymbol{q}_r, \nu_i\boldsymbol{q}_i) = p_\sigma(\nu_r\boldsymbol{q}_r, \nu_i\boldsymbol{q}_i)/p_0(\nu_r\boldsymbol{q}_r, \nu_i\boldsymbol{q}_i), \tag{18}$$

where $p_0(\nu_r\boldsymbol{q}_r, \nu_i\boldsymbol{q}_i) \geqslant \epsilon$ and $\epsilon$ is equal to a small numerical constant that corresponds to the minimum nonzero probability of specular reflection ($q_r^{\parallel} = q_i^{\parallel}$) when $\sigma = 0$. This is done to exclude scattering processes in which specular reflection is forbidden (e.g., TA $\rightarrow$ LA scattering for $\theta_i > \theta_c$). In our case, we obtain reasonable results for $\epsilon = 10^{-6}$. To compute $p_\sigma(\nu_r\boldsymbol{q}_r, \nu_i\boldsymbol{q}_i)$ for each combination of $L$ and $\sigma$, we use an ensemble of $N = 20$ realizations of the graphene rough boundary for the ensemble averages in Eq. (5).

If the Ogilvy formula from Eq. (3) holds, it implies that $\zeta_\sigma(\nu_r\boldsymbol{q}_r, \nu_i\boldsymbol{q}_i) = \exp[-\sigma^2(|q_i^{\perp}| + |q_r^{\perp}|)^2]$ or $|\log[\zeta_\sigma(\nu_r\boldsymbol{q}_r, \nu_i\boldsymbol{q}_i)]|^{1/2} \propto \sigma$. Therefore, we define the dimensionless *attenuation parameter* as $\chi(\nu_r\boldsymbol{q}_r, \nu_i\boldsymbol{q}_i) = |\log\zeta_\sigma(\nu_r\boldsymbol{q}_r, \nu_i\boldsymbol{q}_i)|^{1/2}$ or

$$\chi(\nu_r\boldsymbol{q}_r, \nu_i\boldsymbol{q}_i) = \left|\log\left[\frac{p_\sigma(\nu_r\boldsymbol{q}_r, \nu_i\boldsymbol{q}_i)}{p_0(\nu_r\boldsymbol{q}_r, \nu_i\boldsymbol{q}_i)}\right]\right|^{1/2} \tag{19}$$

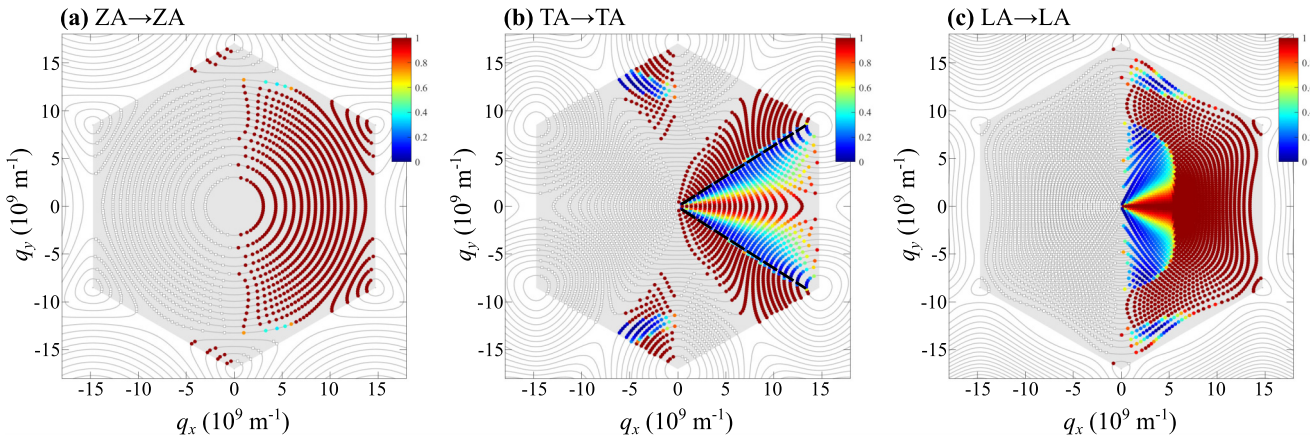


FIG. 3. Plot of the probability of specular reflectance $p_0(\nu_r \boldsymbol{q}_r, \nu_i \boldsymbol{q}_i)$ with no mode conversion ($\nu_r = \nu_i$ and $|q_r^\perp| = |q_i^\perp|$) by a perfect ($\sigma = 0$) zigzag-edge graphene boundary for the (a) ZA, (b) TA, and (c) LA phonons distributed over the first Brillouin zone (gray-shaded region). Each solid circle at $\boldsymbol{q}_i = (q_x, q_y)$ in the Brillouin zone corresponds to an incident rightward-propagating phonon mode, with its color representing the value of $p_0(\nu_r \boldsymbol{q}_r, \nu_i \boldsymbol{q}_i)$. Because only rightward-propagating phonon modes are indicated, only half of the BZ is covered by the solid circles. The other half of the BZ is covered by hollow circles corresponding to the leftward-propagating phonon modes that cannot scatter with the boundary. The phonon modes are located on the frequency contours (gray solid lines) drawn at intervals of $\Delta\omega = 0.5 \times 10^{13}$ rad/s like in Fig. 2. The critical angle $\theta_c$ for the mode conversion of the TA phonons is indicated by the black dashed line in (b).

to characterize the degree of attenuation from boundary roughness scattering in our simulation results. If the Ogilvy formula holds, then we have $\zeta_\sigma(\nu_r \boldsymbol{q}_r, \nu_i \boldsymbol{q}_i) = \exp[-\chi(\nu_r \boldsymbol{q}_r, \nu_i \boldsymbol{q}_i)^2]$ and we may regard Eq. (19) as a generalization of the Rayleigh roughness parameter $\Sigma$ from Eq. (1) since $\Sigma = \frac{1}{2}\chi$. If there is no attenuation, then $\chi = 0$; if specular reflection is totally eliminated, then $\chi = \infty$. For Eq. (19), we have $|q_r^\perp| = |q_i^\perp|$ in the absence of mode conversion ($\nu_r = \nu_i$) and $|q_r^\perp| \neq |q_i^\perp|$ otherwise ($\nu_r \neq \nu_i$). For convenience, we define the average of the normal component of the incident and reflected wave vectors as

$$Q_x = \frac{|q_i^\perp| + |q_r^\perp|}{2} \tag{20}$$

to obtain the expression $\zeta_\sigma(\nu_r \boldsymbol{q}_r, \nu_i \boldsymbol{q}_i) = \exp[-4\sigma^2 Q_x^2]$ or $\chi(\nu_r \boldsymbol{q}_r, \nu_i \boldsymbol{q}_i) = 2\sigma Q_x$ from Eq. (3). We note that $Q_x$ is a function of $\boldsymbol{q}_i$ and hence $q_x$ since $q_i^\perp = q_x$ and $q_r^\perp$ is uniquely determined by $q_i^\perp$ when $\nu_r$ and $\nu_i$ are given. If there is no mode conversion ($\nu_r = \nu_i$), then $Q_x = |q_x|$ because $q_r^\perp = q_i^\perp$. Conversely, if there is mode conversion ($\nu_r \neq \nu_i$), then $Q_x \neq |q_x|$.

### B. Specular reflection for no boundary roughness ($\sigma = 0$)

To apply Eq. (3), we first compute the probability of specular reflectance $p_0(\nu_r \boldsymbol{q}_r, \nu_i \boldsymbol{q}_i)$, which will serve as the baseline case when there is no boundary roughness ($\sigma = 0$ or $\mathcal{T} = 0$), with and without mode conversion. The $p_0(\nu_r \boldsymbol{q}_r, \nu_i \boldsymbol{q}_i)$ data also tell us which specular scattering processes with or without mode conversion are allowed and which ones are forbidden.

In Fig. 3, we plot $p_0(\nu_r \boldsymbol{q}_r, \nu_i \boldsymbol{q}_i)$ with no mode conversion, where $\nu_r = \nu_i$ and $|q_r^\perp| = |q_i^\perp|$, for incident (a) ZA, (b) TA, and (c) LA phonons in zigzag-edge graphene. The data in Figs. 3(a)–3(c) correspond to the ZA → ZA, TA → TA, and LA → LA scattering processes, respectively. In Fig. 3, each solid circle is located at $(q_x, q_y)$ and is associated with an *incoming* phonon mode that has the wave vector $\boldsymbol{q}_i = (q_x, q_y)$ within the first Brillouin zone and a velocity component ($v_x$) that is directed rightwards towards the boundary, i.e., $v_x > 0$. The phonon modes that have a leftward velocity component ($v_x < 0$) are not shown because they are associated with the *outgoing* phonon modes reflected by the boundary. Because the calculations of the $S$ matrices are performed in steps of $\omega$, we obtain a set of $p_0(\nu_r \boldsymbol{q}_r, \nu_i \boldsymbol{q}_i)$ values for each $\omega$ value which we can see in Fig. 3 where the data point for each phonon mode is located on one of the frequency contour lines.

For the ZA phonons [Fig. 3(a)], the value of $p_0$ is almost uniformly equal to unity within the BZ, indicating an absence of mode conversion in boundary scattering, which we attribute to the planar symmetry of SLG. On the other hand, for the TA phonons [Fig. 3(b)], the value of $p_0$ deviates significantly from unity, indicating the presence of TA → LA mode conversion, when the angle of incidence $\theta_i$ is smaller than the critical angle $\theta_c$, which is indicated by the black solid line in Fig. 3(b) and given by $\sin\theta_c = c_T/c_L$. As $\theta_i$ approaches zero (normal incidence), the degree of mode conversion for the TA phonons decreases and converges to zero at $\theta_i = 0$. When $\theta_i > \theta_c$, the value of $p_0$ is unity almost everywhere in the BZ, indicating the absence of mode conversion. For the LA phonons [Fig. 3(c)], LA → TA mode conversion is not angle-limited because $c_L > c_T$ but has a sharp frequency cutoff because the process is limited by the maximum frequency of the TA phonons at the edge of the BZ ($\omega = 1.5 \times 10^{14}$ rad/s). Like the case for TA phonons, the degree of mode conversion converges to zero as $\theta_i$ approaches zero.

Similarly, in Fig. 4, we plot $p_0(\nu_r \boldsymbol{q}_r, \nu_i \boldsymbol{q}_i)$ with only mode conversion ($\nu_r \neq \nu_i$ and $|q_r^\perp| \neq |q_i^\perp|$) for the TA and LA phonons, with the data corresponding to the TA→LA and LA→TA scattering processes. We do not plot $p_0(\nu_r \boldsymbol{q}_r, \nu_i \boldsymbol{q}_i)$ for the ZA phonons because they cannot undergo mode conversion, i.e., there are no ZA → LA or ZA → TA scattering processes due to the planar symmetry of the SLG boundary. As expected, the results in Figs. 4(a) and 4(b) are

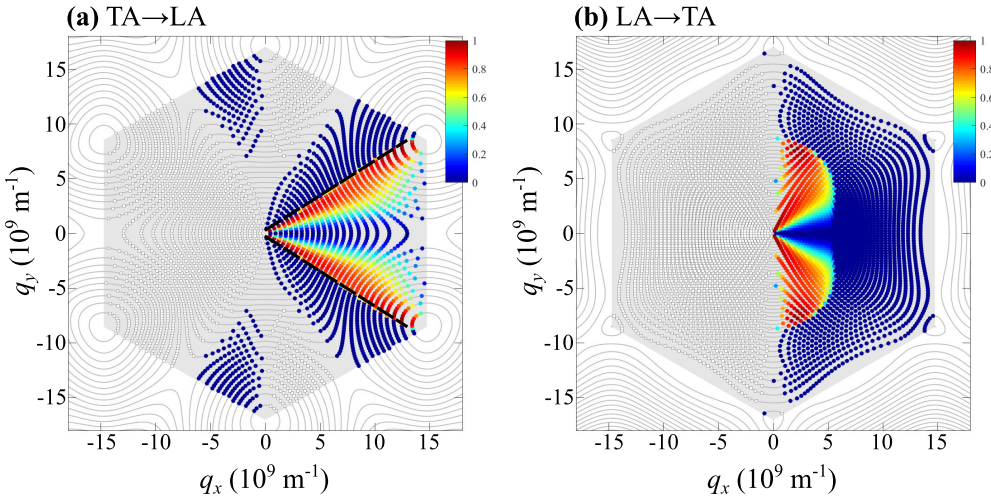


FIG. 4. Plot of the probability of specular reflectance $p_0(\nu_r \boldsymbol{q}_r, \nu_i \boldsymbol{q}_i)$ with only mode conversion ($\nu_r \neq \nu_i$ and $|q_r^\perp| \neq |q_i^\perp|$) by a perfect ($\sigma = 0$) zigzag-edge graphene boundary for the (a) TA and (b) LA phonons distributed over the first Brillouin zone (gray-shaded region). Each solid circle at $\boldsymbol{q}_i = (q_x, q_y)$ in the Brillouin zone corresponds to an incident rightward-propagating phonon mode, with its color representing the value of $p_0(\nu_r \boldsymbol{q}_r, \nu_i \boldsymbol{q}_i)$. Like in Figs. 2 and 3, the frequency contours are drawn at intervals of $\Delta\omega = 0.5 \times 10^{13}$ rad/s. The critical angle $\theta_c$ for the mode conversion of the TA phonons is indicated by the black dashed line in (a).

complementary and opposite to those in Figs. 3(b) and 3(c). The values of $p_0$ with only mode conversion are nonzero for the TA phonons when $\theta_i < \theta_c$ and converge to zero as $\theta_i$ approaches zero. Similarly, the values of $p_0$ with only mode conversion are nonzero for the LA phonons when $\theta_i < \pi/2$ and converge to zero as $\theta_i$ approaches zero.

### C. Specular reflection for finite boundary roughness ($\sigma \neq 0$)

To investigate the effects of boundary roughness scattering, we compute $p_\sigma(\nu_r \boldsymbol{q}_r, \nu_i \boldsymbol{q}_i)$ with and without mode conversion for the ZA, TA, and LA phonons and boundary structures at different values of the lateral correlation length $L$ and boundary roughness $\sigma$. We quantify the effects by analyzing the reciprocal-space distribution of $p_\sigma(\nu_r \boldsymbol{q}_r, \nu_i \boldsymbol{q}_i)$ and $\chi(\nu_r \boldsymbol{q}_r, \nu_i \boldsymbol{q}_i)$ from Eqs. (5) and (19), respectively. Three sets of boundary structures with different $\sigma$ and $L$ values are used in our simulations. The first set has $\sigma = 0.5R_0$ and $L = L_0$ and describes boundary structures with a small boundary roughness and small correlation length. The second set has $\sigma = 1.5R_0$ and $L = L_0$ and describes boundary structures with a large boundary roughness and small correlation length. We use the contrast between the first and second set to investigate the change in $\chi$ when the boundary roughness is increased. The third set $\sigma = 0.5R_0$ and $L = 8L_0$ and describes boundary structures with a small boundary roughness and large correlation length. The third set describes a much smoother boundary and is used to investigate the change in $\chi$ when the lateral correlation length is larger.

#### *1. Small lateral correlation length and small roughness*

In Fig. 5, we plot $p_\sigma(\nu_r \boldsymbol{q}_r, \nu_i \boldsymbol{q}_i)$ with *no mode conversion* ($\nu_r = \nu_i$ and $|q_r^\perp| = |q_i^\perp|$) for the (a) ZA, (b) TA, and (c) LA phonons at a small correlation length ($L = L_0$) and small boundary roughness ($\sigma = 0.5R_0$). Like in Fig. 3, the $p_\sigma$ data in Figs. 5(a)–5(c) correspond to the ZA → ZA, TA → TA, and LA → LA scattering processes, respectively. The topographic parameter for this boundary structure is $\mathcal{T} = \frac{1}{\sqrt{3}}$, which suggests that the Ogilvy formula should be valid. By comparing the $p_\sigma$ data in Figs. 5(a)–5(c) to the $p_0$ data in Figs. 3(a)–3(c), we can observe the effects of boundary roughness scattering on specular reflection ($q_r^\parallel = q_i^\parallel$). As expected, the values of $p_\sigma(\nu_r \boldsymbol{q}_r, \nu_i \boldsymbol{q}_i)$ are markedly attenuated by boundary roughness scattering, in contrast to the results for $p_0$ in Figs. 3(a)–3(c). To analyze this attenuation in the specular reflection, we also plot the corresponding values of $\chi(\nu_r \boldsymbol{q}_r, \nu_i \boldsymbol{q}_i)$ from Eq. (19) as a function of $Q_x$ from Eq. (20) in Figs. 5(d)–5(f). In the absence of mode conversion, we have $Q_x = |q_i^\perp| = q_x$.

To compare the $\chi(\nu_r \boldsymbol{q}_r, \nu_i \boldsymbol{q}_i)$ data and the Ogilvy formula from Eq. (3), we also draw in Figs. 5(d)–5(f) two lines going from the origin to $Q_x = \frac{\pi}{4\sigma}$, which is the maximum value of $Q_x$ at which Eq. (3) is expected to hold as implied by the Rayleigh roughness criterion [15]. The first line, which is based on the RMS boundary roughness $\sigma$ from Eq. (6) used to construct the atomistic graphene boundary like in Fig. 1, is labeled "Geometrical" and given by $2\sigma Q_x$. The second line ("Effective") is a linear fit of the $\chi$ data between $0 < Q_x < \frac{\pi}{4\sigma}$ through the origin, from which we extract the parameter

$$\rho_{\text{fit}} = \frac{\chi(\nu_r \boldsymbol{q}_r, \nu_i \boldsymbol{q}_i)}{2Q_x}. \tag{21}$$

Equation (21) describes the *effective* boundary roughness associated with phonon scattering as described by Eq. (18). We compare $\sigma$ and $\rho_{\text{fit}}$ to analyze the degree of agreement between the geometrical boundary roughness $\sigma$, which describes scalar wave scattering, and the effective boundary roughness $\rho_{\text{fit}}$ deduced from the $\chi$ data. Strictly speaking, the Ogilvy formula is only valid in the $\frac{1}{L} < Q_x < \frac{\pi}{4\sigma}$ range, which we indicate in the yellow-shaded region in Figs. 5(d)–5(f).

In Figs. 5(d)–5(f), we observe a close agreement between $\sigma$ and $\rho_{\text{fit}}$. When $Q_x < \frac{\pi}{4\sigma}$ and especially in the narrower

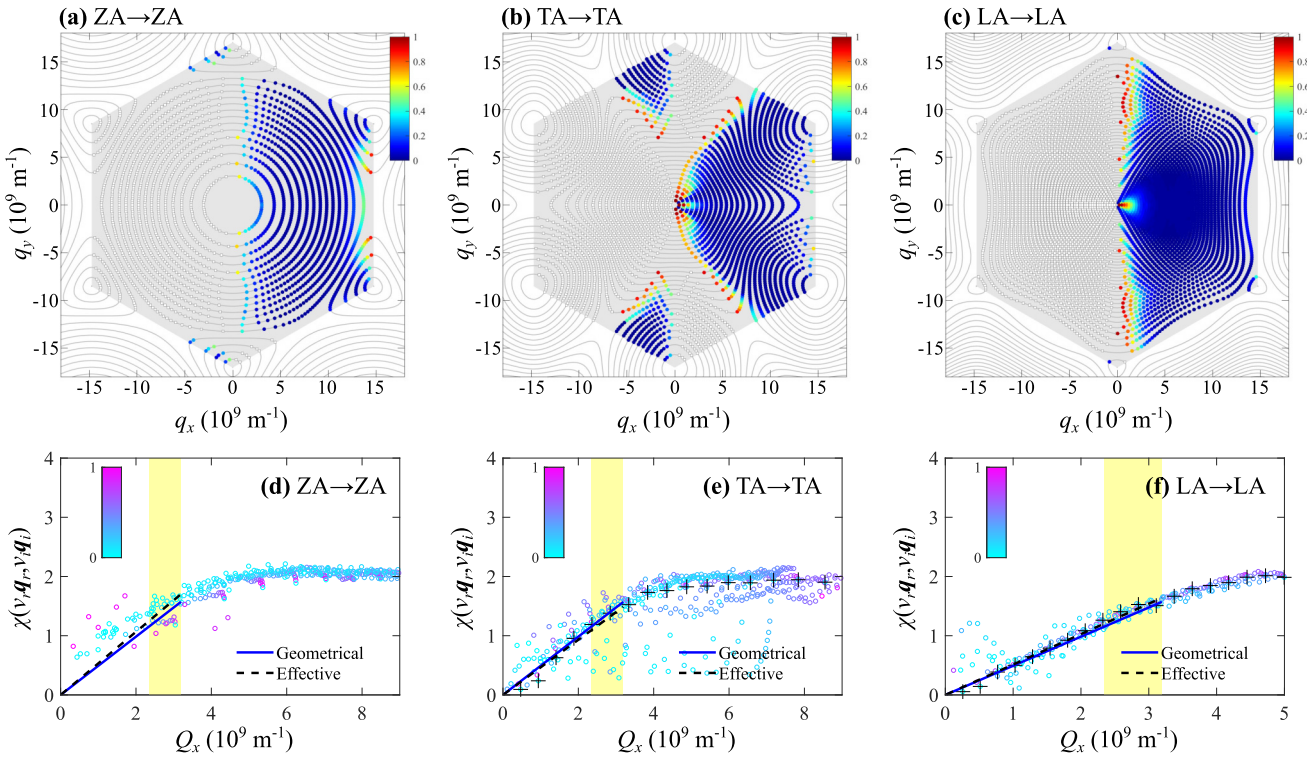


FIG. 5. Plot of the probability of specular reflectance $p_\sigma(\nu_r \boldsymbol{q}_r, \nu_i \boldsymbol{q}_i)$ with no mode conversion ($\nu_r = \nu_i$ and $|q_r^\perp| = |q_i^\perp|$) for the (a) ZA, (b) TA, and (c) LA phonons, distributed over the first Brillouin zone, for $\sigma = 0.5R_0$ and $L = L_0$ ($\mathcal{T} = \frac{1}{\sqrt{3}}$). The value of each $p_\sigma(\nu_r \boldsymbol{q}_r, \nu_i \boldsymbol{q}_i)$ is indicated in color according to the color bar in the top right corner of each panel. The corresponding data for $\chi(\nu_r \boldsymbol{q}_r, \nu_i \boldsymbol{q}_i)$ vs $Q_x$ are shown as hollow circles in panels (d)–(f). The corresponding angle of incidence $\theta_i$ of each $\chi$ data point (normalized by $\pi/2$) is indicated by color according to the color bar in the top left corner of each panel, with 0 and 1 corresponding to normal and grazing incidence. Two linear fits are drawn for $0 < Q_x < \frac{\pi}{4\sigma}$: the "Geometrical" (solid blue line) and the "Effective" (dashed black line). The range for $\frac{1}{L} < Q_x < \frac{\pi}{4\sigma}$ is indicated by the yellow-shaded region. For the TA and LA phonons, the data points for $\theta_i = 0$ (normal incidence) are also indicated by the "+" symbol.

$\frac{1}{L} < Q_x < \frac{\pi}{4\sigma}$ range, the Ogilvy formula describes the behavior of $\chi(\nu_r \boldsymbol{q}_r, \nu_i \boldsymbol{q}_i)$, which increases linearly with $Q_x$. This implies that the Ogilvy formula provides a good description of the attenuation of the specularity parameter for ZA, TA, and LA phonons if there is no mode conversion. For $Q_x > \frac{\pi}{4\sigma}$, the Rayleigh roughness criterion [15] is no longer satisfied and the derivative of $\chi(\nu_r \boldsymbol{q}_r, \nu_i \boldsymbol{q}_i)$ decreases substantially, with the value of $\chi(\nu_r \boldsymbol{q}_r, \nu_i \boldsymbol{q}_i)$ plateauing at higher values of $Q_x$. This plateauing indicates that the boundary roughness-induced attenuation of the specularity parameter is maximized at a limiting value of $Q_x$.

Nonetheless, there is a wide dispersion of the $\chi(\nu_r \boldsymbol{q}_r, \nu_i \boldsymbol{q}_i)$ data points around the $\sigma$ and $\rho_{\text{fit}}$ lines, especially for the TA phonons when $Q_x$ is small. At small $Q_x$ and especially for the LA phonon, the value of $\chi(\nu_r \boldsymbol{q}_r, \nu_i \boldsymbol{q}_i)$ is noticeably higher than that predicted by the Ogilvy formula. This indicates that the attenuation of the specularity is greater than what the Ogilvy formula predicts for these small-$Q_x$ (long-wavelength) phonon modes and implies that the validity of Eq. (3) for describing the specularity attenuation is limited when $L$ is small and outside the $\frac{1}{L} < Q_x < \frac{\pi}{4\sigma}$ range. This is probably due to the $qL \gg 1$ condition associated with the Kirchhoff approximation, which implies that the Ogilvy formula is only valid when the lateral correlation length is much larger than the wavelength.

The dispersion is more pronounced for the TA and LA phonons in Figs. 5(e) and 5(f) but less so for the ZA phonons in Fig. 5(d). In particular for the small-$Q_x$ LA phonons, the $\chi(\nu_r \boldsymbol{q}_r, \nu_i \boldsymbol{q}_i)$ data points can be significantly larger than $2\sigma Q_x$, indicating that the attenuation is greater than what is predicted by the Ogilvy formula. The more pronounced dispersion of the $\chi$ data could be due to the effects of mode conversion (TA → LA and LA → TA) which is absent for the boundary roughness scattering of the ZA phonon. To analyze this, we also replot the $\chi(\nu_r \boldsymbol{q}_r, \nu_i \boldsymbol{q}_i)$ data for $\theta_i = 0$, which correspond to phonons at normal incidence to the boundary, in Figs. 5(e) and 5(f), and we find that they fall very close to the lines for $\sigma$ and $\rho_{\text{fit}}$. The plateauing of $\chi(\nu_r \boldsymbol{q}_r, \nu_i \boldsymbol{q}_i)$ at larger $Q_x$ values is also less ambiguous. This suggests that the Ogilvy formula is more accurate for describing the boundary roughness scattering of phonons at normal incidence to the boundary.

For a more complete picture of the validity of the Ogilvy formula for this boundary structure, we also study the attenuation of $p_\sigma(\nu_r \boldsymbol{q}_r, \nu_i \boldsymbol{q}_i)$ during *mode conversion* ($\nu_r \neq \nu_i$ and $|q_r^\perp| \neq |q_i^\perp|$) in which the polarization of the incident phonon is changed by boundary scattering. Figures 6(a) and 6(b) show the $p_\sigma(\nu_r \boldsymbol{q}_r, \nu_i \boldsymbol{q}_i)$ data with *mode conversion* for the (a) TA and (b) LA phonons. The $p_\sigma$ data in Figs. 6(a) and 6(b) correspond to the TA → LA and LA → TA scattering processes, respectively. The range of incident angles for the TA

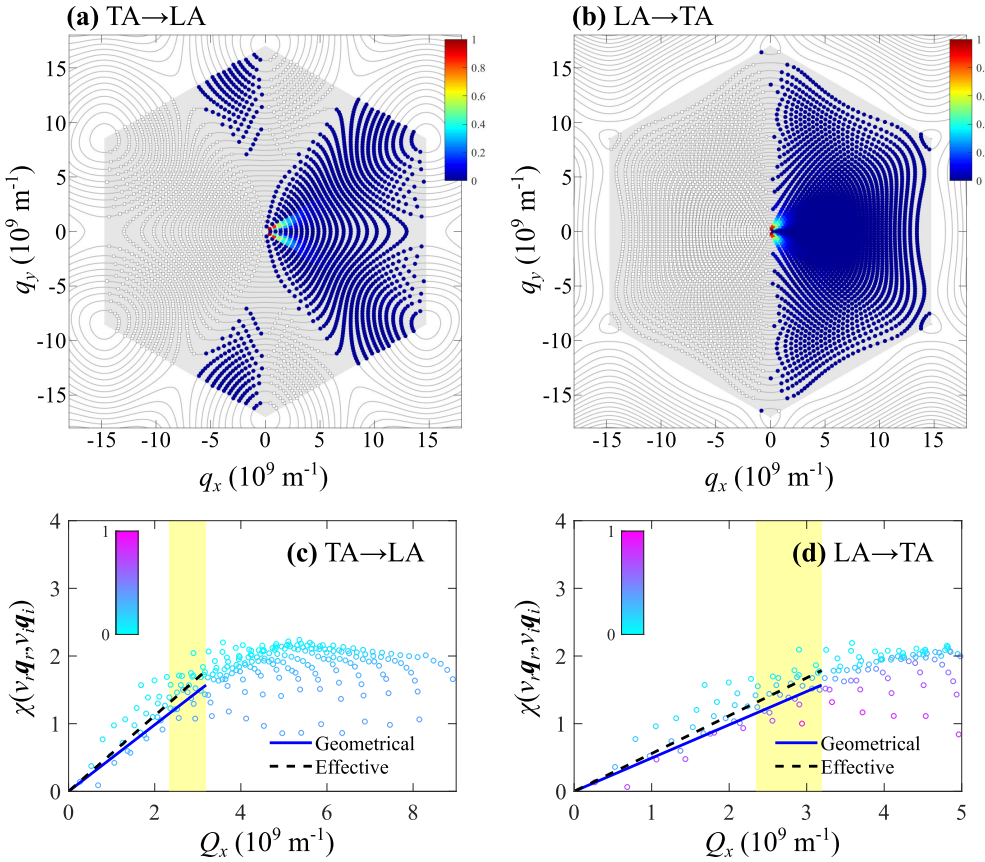


FIG. 6. Plot of the probability of specular reflectance $p_\sigma(\nu_r \boldsymbol{q}_r, \nu_i \boldsymbol{q}_i)$ with mode conversion ($\nu_r \neq \nu_i$ and $|q_r^\perp| \neq |q_i^\perp|$) for incident (a) TA and (b) LA phonons, distributed over the first Brillouin zone, for $\sigma = 0.5R_0$ and $L = L_0$ ($\mathcal{T} = \frac{1}{\sqrt{3}}$). The value of each $p_\sigma(\nu_r \boldsymbol{q}_r, \nu_i \boldsymbol{q}_i)$ is indicated in color according to the color bar in the top right corner of each panel. The corresponding data for $\chi(\nu_r \boldsymbol{q}_r, \nu_i \boldsymbol{q}_i)$ are shown as hollow circles in panels (c) and (d). The corresponding angle of incidence $\theta_i$ of each $\chi$ data point (normalized by $\pi/2$) is indicated by color according to the color bar in the top left corner of each panel.

and LA phonons is given by $0 < \theta_i < \theta_c$ and $0 < \theta_i < \pi/2$, respectively. We also plot the corresponding $\chi(\nu_r \boldsymbol{q}_r, \nu_i \boldsymbol{q}_i)$ data as a function of $Q_x$ in Figs. 6(c) and 6(d).

In Fig. 6, we observe that $\chi(\nu_r \boldsymbol{q}_r, \nu_i \boldsymbol{q}_i)$ increases linearly with $Q_x$ for $Q_x < \frac{\pi}{4\sigma}$ and plateaus at higher values of $Q_x$ like in Figs. 5(e) and 5(f), although there is also a greater dispersion of the data points. We observe that for $Q_x > \frac{\pi}{4\sigma}$, the attenuation of $p_\sigma$ is weaker as the angle of incidence $\theta_i$ increases. We also find that the extracted value for the effective boundary roughness $\rho_{\text{fit}}$ is also close but slighter larger than the geometrical boundary roughness $\sigma$ for both the TA and LA phonons. Compared to Figs. 5(e) and 5(f), there is a smaller dispersion of the $\chi(\nu_r \boldsymbol{q}_r, \nu_i \boldsymbol{q}_i)$ data points around the $\rho_{\text{fit}}$ and $\sigma$ lines. This suggests that the Ogilvy formula provides a better description of the specularity attenuation from boundary roughness scattering for scattering processes that involve mode conversion (e.g. TA → LA and LA → TA). In addition, we notice a noticeable dependence of $\chi$ on the angle of incidence $\theta_i$ especially when $Q_x > \frac{\pi}{4\sigma}$. For the same $Q_x$ but higher $\theta_i$ (or more oblique angle), $\chi(\nu_r \boldsymbol{q}_r, \nu_i \boldsymbol{q}_i)$ is smaller even though the Ogilvy formula from Eq. (3) implies that it should only depend on $Q_x$.

#### 2. *Small lateral correlation length and large roughness*

To see the effect of a larger boundary roughness, we repeat our analysis of $p_\sigma(\nu_r \boldsymbol{q}_r, \nu_i \boldsymbol{q}_i)$ with *no mode conversion* for the (a) ZA, (b) TA, and (c) LA phonons at the same small correlation length ($L = L_0$) as in Sec. III C 1 but a larger boundary roughness ($\sigma = 1.5R_0$). The results are shown in Fig. 7. The topographic parameter for this boundary structure is $\mathcal{T} = \sqrt{3}$, which suggests that the Ogilvy formula in Eq. (3) should *not* be valid at all. Nevertheless, it would be interesting to compare the degree of agreement between the corresponding $\chi(\nu_r \boldsymbol{q}_r, \nu_i \boldsymbol{q}_i)$ data and the Ogilvy formula. The data for $\chi(\nu_r \boldsymbol{q}_r, \nu_i \boldsymbol{q}_i)$ are shown in Figs. 7(d)–7(f). Although we have $\mathcal{T} = \sqrt{3}$, there is nonetheless some qualitative agreement between the Ogilvy formula and the data. We observe that $\chi(\nu_r \boldsymbol{q}_r, \nu_i \boldsymbol{q}_i)$ increases with $Q_x$ up to $Q_x = \frac{\pi}{4\sigma}$, although there is greater dispersion of the $\chi(\nu_r \boldsymbol{q}_r, \nu_i \boldsymbol{q}_i)$ data points around the lines for $\sigma$ and $\rho_{\text{fit}}$, which we can attribute to the greater $\sigma$.

In Fig. 7(f), which corresponds to LA phonons, the lines for $\sigma$ and $\rho_{\text{fit}}$ are markedly different with the effective roughness $\rho_{\text{fit}}$ being significantly smaller than the geometrical roughness $\sigma$. In particular, we observe that at small $Q_x$, the $\chi(\nu_r \boldsymbol{q}_r, \nu_i \boldsymbol{q}_i)$

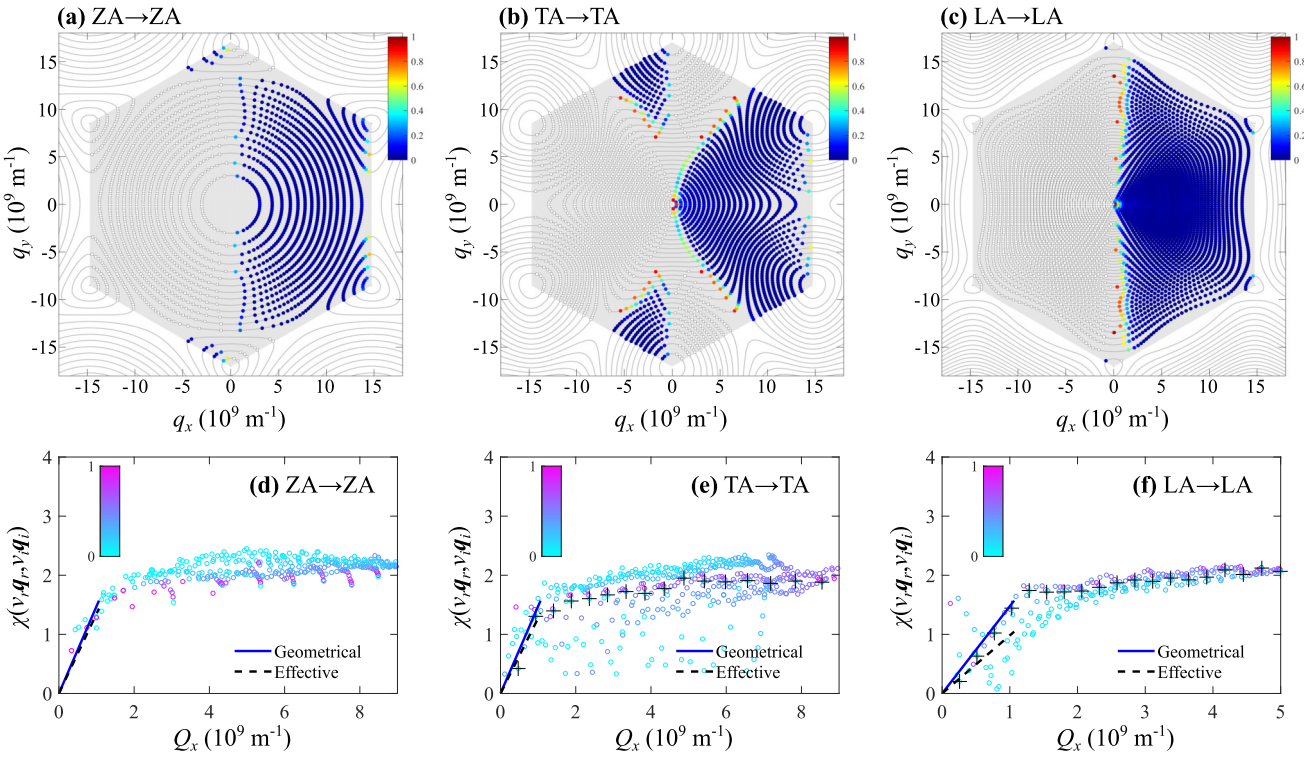


FIG. 7. Plot of the probability of specular reflectance $p_\sigma(\nu_r \boldsymbol{q}_r, \nu_i \boldsymbol{q}_i)$ with no mode conversion ($\nu_r = \nu_i$ and $|q_r^\perp| = |q_i^\perp|$) for incident (a) ZA, (b) TA, and (c) LA phonons, distributed over the first Brillouin zone, for $\sigma = 1.5R_0$ and $L = L_0$ ($\mathcal{T} = \sqrt{3}$). The value of each $p_\sigma(\nu_r \boldsymbol{q}_r, \nu_i \boldsymbol{q}_i)$ is indicated in color according to the color bar in the top right corner of each panel. The corresponding data for $\chi(\nu_r \boldsymbol{q}_r, \nu_i \boldsymbol{q}_i)$ are shown as hollow circles in panels (d)–(f). The corresponding angle of incidence $\theta_i$ of each $\chi$ data point (normalized by $\pi/2$) is indicated by color according to the color bar in the top left corner of each panel. Two linear fits are drawn for $0 < Q_x < \frac{\pi}{4\sigma}$: the "Geometrical" (solid blue line) and the "Effective" (dashed black line). For the TA and LA phonons, the data points for $\theta_i = 0$ (normal incidence) are also indicated by the "+" symbol.

data for smaller $\theta_i$ but not at normal incidence tend to be significantly lower than the values predicted by the Ogilvy formula. In other words, specular reflection of the LA phonons is less attenuated than predicted for slightly oblique angles. The $\chi(\nu_r \boldsymbol{q}_r, \nu_i \boldsymbol{q}_i)$ data for normal incidence or $\theta_i = 0$, however, show a much closer fit to the line for $\sigma$. This suggests that the Ogilvy formula in Eq. (3) retains some accuracy for describing the effects of boundary roughness scattering on the specularity, especially for phonons at normal incidence, even when the boundary roughness and topographic parameter are large enough to invalidate the Ogilvy formula.

Figure 8 shows the data for $p_\sigma(\nu_r \boldsymbol{q}_r, \nu_i \boldsymbol{q}_i)$ with *mode conversion* ($\nu_r \neq \nu_i$ and $|q_r^\perp| \neq |q_i^\perp|$) for the (a) TA and (b) LA phonons for the same boundary structure. Qualitatively, like in Fig. 7, we observe that $\chi(\nu_r \boldsymbol{q}_r, \nu_i \boldsymbol{q}_i)$ increases with $Q_x$ for $Q_x < \frac{\pi}{4\sigma}$. For $Q_x > \frac{\pi}{4\sigma}$, we similarly observe that the maximum value of $\chi(\nu_r \boldsymbol{q}_r, \nu_i \boldsymbol{q}_i)$ plateaus with $Q_x$ although there are $\chi(\nu_r \boldsymbol{q}_r, \nu_i \boldsymbol{q}_i)$ data points in Figs. 8(c) and 8(d) that are significantly below the plateau line. Like in Fig. 6, we similarly observe that for $Q_x > \frac{\pi}{4\sigma}$, the attenuation of $p_\sigma$ is weaker as $\theta_i$ increases or becomes closer to the grazing angle. This implies that $\chi(\nu_r \boldsymbol{q}_r, \nu_i \boldsymbol{q}_i)$ has a dependence on $\theta_i$ in addition to its dependence on $Q_x$ when $\mathcal{T}$ is large, and that there is an additional dependence on the transverse momentum $q_y$ that is not predicted in the Ogilvy formula. By comparing Figs. 6 and 8, we observe that this angle-dependent weakening of the attenuation parameter is more pronounced when $\sigma$ is larger.

#### 3. *Large lateral correlation length and small roughness*

At large lateral correlation lengths, the boundary is smoother when $L \gg \sigma$ and $\mathcal{T} \ll 1$. In Fig. 9, we plot $p_\sigma(\nu_r \boldsymbol{q}_r, \nu_i \boldsymbol{q}_i)$ with *no mode conversion* for the (a) ZA, (b) TA, and (c) LA phonons at a large correlation length ($L = 8L_0$) and a small boundary roughness ($\sigma = 0.5R_0$) as in Sec. III C 1. We also plot the corresponding values of $\chi(\nu_r \boldsymbol{q}_r, \nu_i \boldsymbol{q}_i)$ from Eq. (18) in Figs. 9(d)–9(f). Because the corresponding topographic parameter $\mathcal{T} = \frac{1}{8\sqrt{3}} \ll 1$ is much smaller than unity, we expect Eq. (3) to be optimal for describing specularity attenuation by boundary roughness scattering. Thus, by comparing the $\chi(\nu_r \boldsymbol{q}_r, \nu_i \boldsymbol{q}_i)$ data and the Ogilvy formula, we can assess the accuracy of Eq. (3) in the most ideal case.

Compared to the results for a small correlation length ($L = L_0$) and small boundary roughness ($\sigma = 0.5R_0$) in Figs. 5(d)–5(f) where $\mathcal{T} = \frac{1}{\sqrt{3}}$, there is a much smaller dispersion of the $\chi(\nu_r \boldsymbol{q}_r, \nu_i \boldsymbol{q}_i)$ data points around the line for the geometrical boundary roughness $\sigma$, especially for the ZA phonons where most of the $\chi$ data points tend to fall very close to the line when $Q_x < \frac{\pi}{4\sigma}$. In fact, one observes a near-perfect agreement

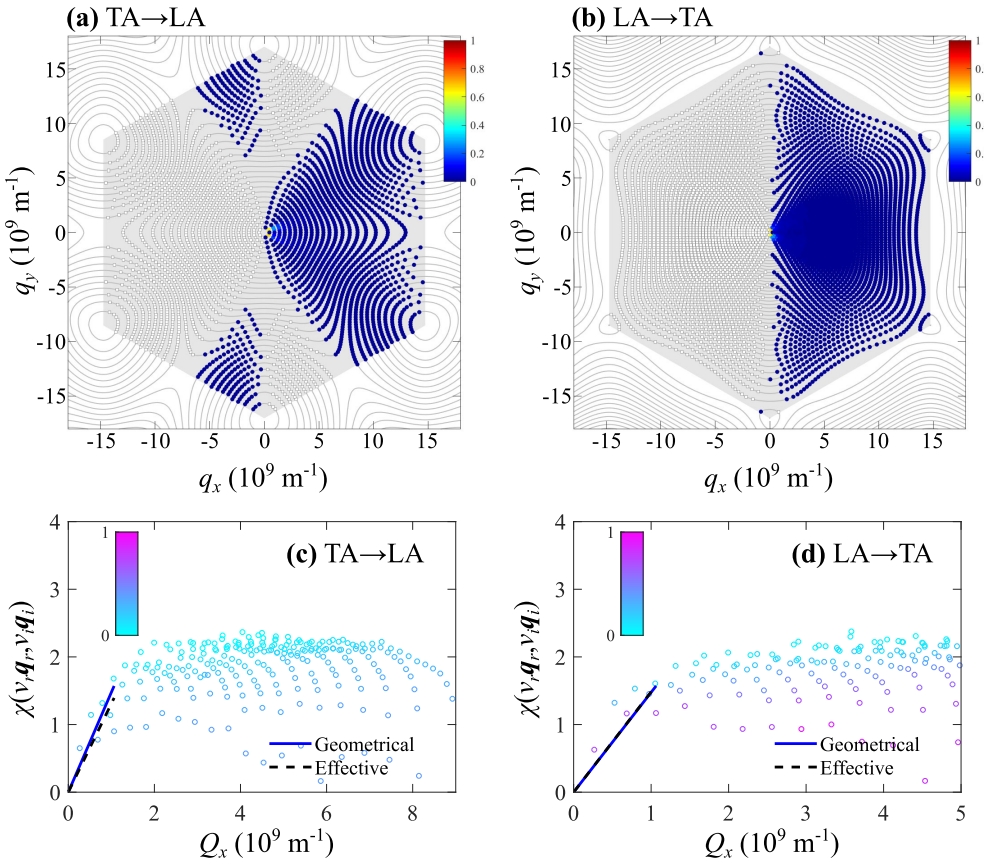


FIG. 8. Plot of the probability of specular reflectance $p_\sigma(\nu_r \boldsymbol{q}_r, \nu_i \boldsymbol{q}_i)$ with mode conversion ($\nu_r \neq \nu_i$ and $|q_r^\perp| \neq |q_i^\perp|$) for the (a) TA and (b) LA phonons, distributed over the first Brillouin zone, for $\sigma = 1.5R_0$ and $L = L_0$ ($\mathcal{T} = \sqrt{3}$). The value of each $p_\sigma(\nu_r \boldsymbol{q}_r, \nu_i \boldsymbol{q}_i)$ is indicated in color according to the color bar in the top right corner of each panel. The corresponding data for $\chi(\nu_r \boldsymbol{q}_r, \nu_i \boldsymbol{q}_i)$ are shown as hollow circles in panels (c) and (d). The corresponding angle of incidence $\theta_i$ of each $\chi$ data point (normalized by $\pi/2$) is indicated by color according to the color bar in the top left corner of each panel.

with Eq. (3) for the ZA phonons when $Q_x < \frac{\pi}{4\sigma}$ even though the ZA phonons have a nonlinear phonon dispersion, with $\omega \propto q^2$ in the long-wavelength limit. Nonetheless, we still observe that at small $Q_x$ for LA phonons in Fig. 9(f), the value of $\chi(\nu_r \boldsymbol{q}_r, \nu_i \boldsymbol{q}_i)$ is noticeably higher than that predicted by the Ogilvy formula, i.e., the specularity of the small-$Q_x$ modes is more strongly attenuated than what is predicted by the Ogilvy formula. This is similar to what we observe in Fig. 5(f) for a smaller lateral correlation length ($L = L_0$).

The geometrical and effective boundary roughness values $\sigma$ and $\rho_{\text{fit}}$ are also in good agreement. Qualitatively, Figs. 9(d)–9(f) suggest that the agreement with the Ogilvy formula in Eq. (3) is greater when the lateral correlation length $L$ is large. This is expected since Eq. (3) is derived assuming that the correlation length is much greater than the wavelength or $qL \gg 1$. In addition, Figs. 9(e) and 9(f) show that for TA and LA phonons, the $\chi(\nu_r \boldsymbol{q}_r, \nu_i \boldsymbol{q}_i)$ data points for $\theta_i = 0$ also have excellent agreement with Eq. (3).

Beyond the $Q_x = \frac{\pi}{4\sigma}$ point, we observe a clear plateauing of $\chi(\nu_r \boldsymbol{q}_r, \nu_i \boldsymbol{q}_i)$ at a maximum value of $\chi \sim \frac{\pi}{2}$, similar to that in Figs. 5(d)–5(f) where $L$ is smaller. This suggests that relative to $p_0$, there possibly exists a minimum value for $p_\sigma$ associated with the maximum attenuation of short-wavelength acoustic phonons, which we can estimate as

$$\lim_{q_i^\perp \to \infty} p_\sigma(\nu_r \boldsymbol{q}_r, \nu_i \boldsymbol{q}_i) \sim p_0(\nu_r \boldsymbol{q}_r, \nu_i \boldsymbol{q}_i) \exp\left(-\frac{\pi^2}{4}\right). \quad (22)$$

If the minimum $p_\sigma$ in Eq. (22) does exist, it leads to the question of whether this phenomenon is peculiar to the boundary roughness scattering of short-wavelength phonons or if it can be generalized to the boundary roughness scattering of other quasiparticles or waves in general. In the context of phonon-mediated thermal transport, this implies that a boundary scattering event cannot completely dissipate all the momentum of the incident phonon.

Figure 10 shows the corresponding data for $p_\sigma(\nu_r \boldsymbol{q}_r, \nu_i \boldsymbol{q}_i)$ with *mode conversion* ($\nu_r \neq \nu_i$ and $|q_r^\perp| \neq |q_i^\perp|$) for the (a) TA and (b) LA phonons in the same boundary structure. We also plot $\chi(\nu_r \boldsymbol{q}_r, \nu_i \boldsymbol{q}_i)$ for (a) TA and (b) LA phonons. When $Q_x < \frac{\pi}{4\sigma}$, the $\chi(\nu_r \boldsymbol{q}_r, \nu_i \boldsymbol{q}_i)$ data points are in near-perfect agreement with Eq. (3), clustering close to the lines for $\sigma$ and $\rho_{\text{fit}}$. This can be contrasted to the results in Figs. 9(e) and 9(f) for the TA → TA and LA → LA scattering processes, respectively. We also observe the plateauing of the $\chi(\nu_r \boldsymbol{q}_r, \nu_i \boldsymbol{q}_i)$ data points when $Q_x > \frac{\pi}{4\sigma}$. Unlike the results in Figs. 6 and 8 for $L = L_0$, the attenuation of $p_\sigma$ does not vary significantly with the

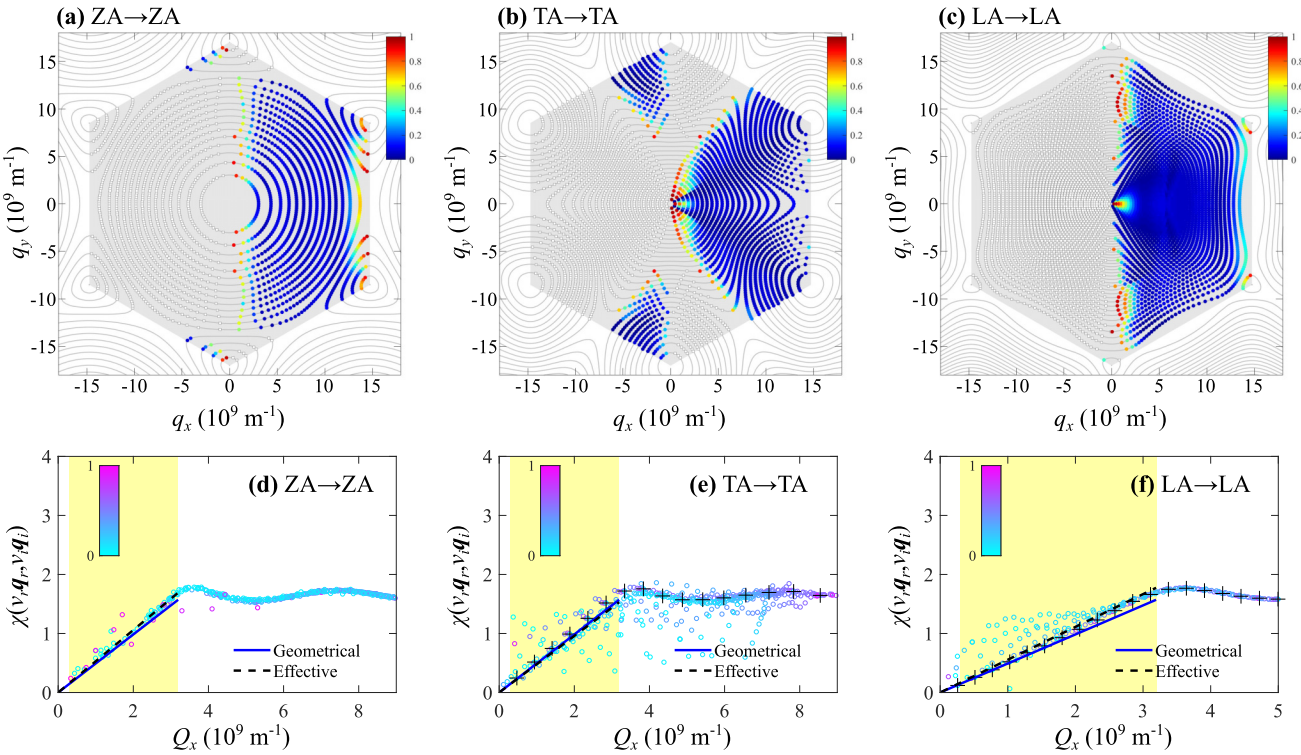


FIG. 9. Plot of the probability of specular reflectance $p_\sigma(\nu_r \boldsymbol{q}_r, \nu_i \boldsymbol{q}_i)$ with no mode conversion ($\nu_r = \nu_i$ and $|q_r^\perp| = |q_i^\perp|$) for the (a) ZA, (b) TA, and (c) LA phonons, distributed over the first Brillouin zone, for $\sigma = 0.5R_0$ and $L = 8L_0$ ($\mathcal{T} = \frac{1}{8\sqrt{3}}$). The value of each $p_\sigma(\nu_r \boldsymbol{q}_r, \nu_i \boldsymbol{q}_i)$ is indicated in color according to the color bar in the top right corner of each panel. The corresponding data for $\chi(\nu_r \boldsymbol{q}_r, \nu_i \boldsymbol{q}_i)$ vs $Q_x$ are shown as hollow circles in panels (d)–(f). The corresponding angle of incidence $\theta_i$ of each $\chi$ data point (normalized by $\pi/2$) is indicated by color according to the color bar in the top left corner of each panel. Two linear fits are drawn for $0 < Q_x < \frac{\pi}{4\sigma}$: the "Geometrical" (solid blue line) and the "Effective" (dashed black line). For the TA and LA phonons, the data points for $\theta_i = 0$ (normal incidence) are also indicated by the "+" symbol.

angle of incidence $\theta_i$ for $Q_x > \frac{\pi}{4\sigma}$ in Fig. 10. This suggests that the additional $\theta_i$-dependence of the $\chi(\nu_r \boldsymbol{q}_r, \nu_i \boldsymbol{q}_i)$ data seen in Figs. 6 and 8 becomes more pronounced as the topographic parameter $\mathcal{T}$ increases.

Given the small $\mathcal{T}$, the results in Figs. 9 and 10 show that the Ogilvy formula is generally excellent for describing the specularity attenuation by boundary roughness scattering except when there is significant possible mode conversion between the phonons involved as with the TA and LA phonons. In the latter case, the formula appears to work better to describe boundary roughness scattering with mode conversion (TA → LA and LA → TA) than for scattering processes without mode conversion (LA → LA and TA → TA). When there is no possible mode conversion (e.g., ZA→ ZA or TA→ TA and LA→ LA at normal incidence), the Ogilvy formula is also more accurate.

## IV. SUMMARY AND CONCLUSIONS

For the convenience of the reader, we summarize our findings from the simulation results from Sec. III. In our simulations, we distinguish and investigate two types of scattering processes—those without mode conversion (ZA → ZA, TA → TA, and LA → LA) and those with mode conversion (TA → LA and LA → TA)—for different boundary structures characterized by the structural parameters $L$ and $\sigma$. The simulation results are benchmarked to the Ogilvy formula from Eq. (3), which describes the attenuation of the specular reflection, and used to determine its dependence on mode conversion and the boundary structural parameters. A notable feature of the Ogilvy formula is that it depends only on the longitudinal component of the incident and reflected wave vectors as given in Eq. (20).

In general, we find that the Ogilvy formula provides a reasonable quantitative description of the attenuation parameter $\chi(\nu_r \boldsymbol{q}_r, \nu_i \boldsymbol{q}_i)$ from Eq. (19), with the data for $\chi$ exhibiting a linear dependence on $Q_x$ (i.e., $\chi \approx 2\rho_{\text{fit}} Q_x$) when $\frac{1}{L} < Q_x < \frac{\pi}{4\sigma}$. We find that the extracted effective boundary roughness $\rho_{\text{fit}}$ is very close to the geometrical boundary roughness $\sigma$ when $\mathcal{T} < 1$. This suggests that the Ogilvy formula applies to the boundary roughness scattering of phonons. As expected, the degree of agreement between the data for $\chi$ and the Ogilvy formula for $Q_x < \frac{\pi}{4\sigma}$ increases as the topographic parameter $\mathcal{T}$ decreases. Nonetheless, even when $\mathcal{T}$ is large (i.e., $\mathcal{T} > 1$), the Ogilvy formula can still describe the linear dependence of $\chi(\nu_r \boldsymbol{q}_r, \nu_i \boldsymbol{q}_i)$ on $Q_x$ very well for phonon modes at normal incidence ($\theta_i = 0$) to the boundary.

Beyond the $Q_x = \frac{\pi}{4\sigma}$ point, the value of $\chi$ plateaus at larger values of $Q_x$ with the asymptotic value of $\chi$ associated with a *possible* minimum $p_\sigma$ value relative to $p_0$. This plateauing is more obvious when $\mathcal{T} \ll 1$. Hence, when $\mathcal{T}$ is small, our results suggest that there are two observable

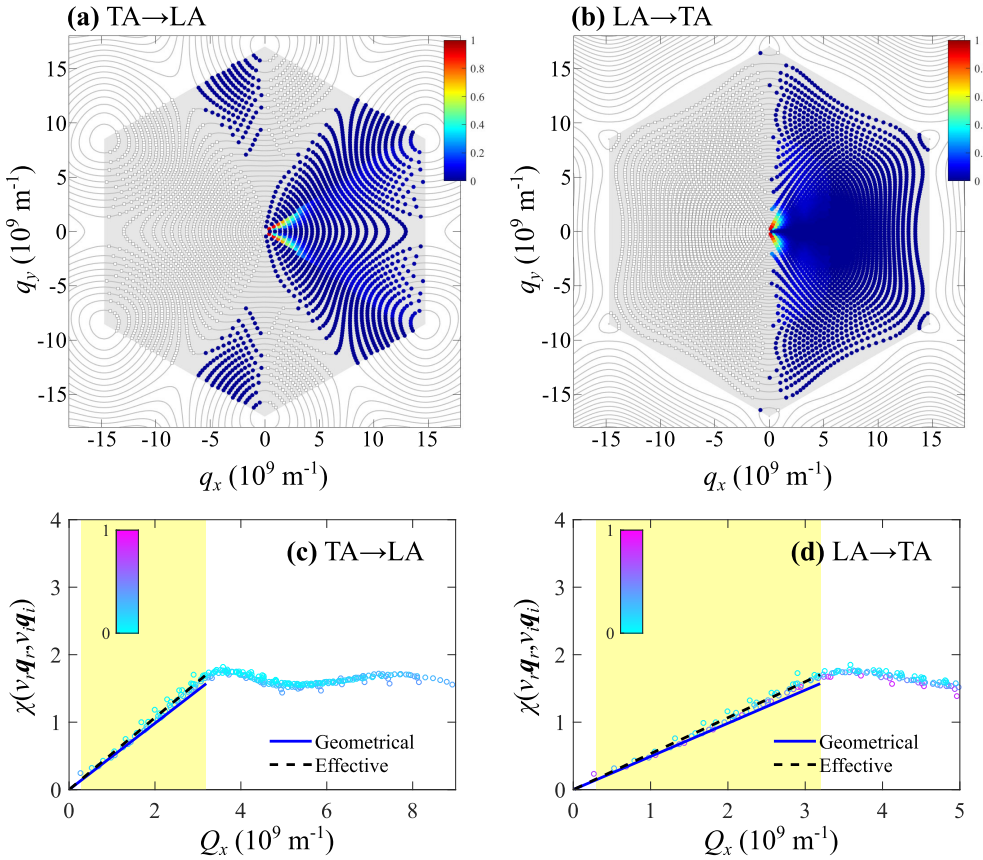


FIG. 10. Plot of the probability of specular reflectance $p_\sigma(\nu_r \boldsymbol{q}_r, \nu_i \boldsymbol{q}_i)$ with mode conversion ($\nu_r \neq \nu_i$ and $|q_r^\perp| \neq |q_i^\perp|$) for the (a) TA and (b) LA phonons, distributed over the first Brillouin zone, for $\sigma = 0.5R_0$ and $L = 8L_0$ ($\mathcal{T} = \frac{1}{8\sqrt{3}}$). The value of each $p_\sigma(\nu_r \boldsymbol{q}_r, \nu_i \boldsymbol{q}_i)$ is indicated in color according to the color bar in the top right corner of each panel. The corresponding data for $\chi(\nu_r \boldsymbol{q}_r, \nu_i \boldsymbol{q}_i)$ are shown as hollow circles in panels (c) and (d). The corresponding angle of incidence $\theta_i$ of each $\chi$ data point (normalized by $\pi/2$) is indicated by color according to the color bar in the top left corner of each panel.

regimes for $\chi$: a linear dependence on $Q_x$ or $\chi \propto Q_x$ for the small-$Q_x$ regime, and an asymptotic convergence to a constant $\chi \sim \frac{\pi}{2}$ for the large-$Q_x$ regime. We conjecture from our numerical results that there exists an *effective minimum specularity value* of $p_\sigma \sim p_0 \exp(-\frac{\pi^2}{4})$ or a maximum attenuation $\chi \sim \frac{\pi}{2}$ for short-wavelength acoustic phonons in the $\mathcal{T} \to 0$ (smooth) limit. This suggests that the momentum of the incident phonon cannot be totally dissipated by boundary scattering.

The effect of mode conversion presents two interesting phenomena. First, in scattering processes without mode conversion (Fig. 9), we find that $\chi$ can be significantly larger than the predicted value of $2\rho_{\text{fit}} Q_x$ at very small $Q_x$ for the LA and TA phonons when $\mathcal{T}$ is small, i.e., the attenuation is significantly stronger than what the Ogilvy formula predicts for long-wavelength phonons. Secondly, in scattering processes that involve mode conversion (LA → LA and TA → TA), at large $Q_x$, $\chi$ can vary independently with the angle of incidence $\theta_i$ with $\chi$ decreasing as $\theta_i$ approaches the grazing angle of $\pi/2$ when $\mathcal{T}$ is large. This implies that the attenuation of the specularity also depends on $q_y$, the transverse component of the incident wave vector. This dependence on $q_y$ also implies that $q_y$-dependent corrections are needed for the Ogilvy formula when $\mathcal{T}$ is large.

In conclusion, our results shed light on the accuracy of the Ogilvy formula in determining the extent that boundary roughness scattering attenuates phonon specular reflection in graphene. They confirm that it is generally accurate for the $Q_x < \frac{\pi}{4\sigma}$ regime when $L$ is large. In the large-$Q_x$ (short-wavelength) regime, they suggest that the Ogilvy formula is not valid and that the attenuation parameter $\chi(\nu_r \boldsymbol{q}_r, \nu_i \boldsymbol{q}_i)$ may exhibit a weak or no dependence on $Q_x$.

## ACKNOWLEDGMENTS

We acknowledge funding support from the Agency for Science, Technology and Research (A*STAR) of Singapore with the Manufacturing, Trade and Connectivity (MTC) Programmatic Grant "Advanced Modeling Models for Additive Manufacturing" (Grant No. M22L2b0111) and from the Polymer Matrix Composites Program (SERC Grant No. A19C9a004). We also acknowledge the assistance of Wen Han Zhang from the National University of Singapore in the preliminary phase of the study. We also acknowledge helpful discussions on the Ogilvy formula with Fan Shi (Hong Kong University of Science and Technology) and Stewart G. Haslinger (University of Liverpool).

[1] S.-M. F. Nee, Polarization of specular reflection and near-specular scattering by a rough surface, Appl. Opt. **35**, 3570 (1996).

[2] B. van Ginneken, M. Stavridi, and J. J. Koenderink, Diffuse and specular reflectance from rough surfaces, Appl. Opt. **37**, 130 (1998).

[3] M. Darmon, V. Dorval, and F. Baqué, Acoustic scattering models from rough surfaces: A brief review and recent advances, Appl. Sci. **10**, 8305 (2020).

[4] R. S. Dwyer-Joyce, B. W. Drinkwater, and A. M. Quinn, The use of ultrasound in the investigation of rough surface interfaces, J. Tribol. **123**, 8 (2001).

[5] S. G. Haslinger, M. J. S. Lowe, R. V. Craster, P. Huthwaite, and F. Shi, Prediction of reflection amplitudes for ultrasonic inspection of rough planar defects, Insight - Non-Destruct. Testing Condition Monitor. **63**, 28 (2021).

[6] J. O. A. Robertsson, R. Laws, C. Chapman, J.-P. Vilotte, and E. Delavaud, Modelling of scattering of seismic waves from a corrugated rough sea surface: a comparison of three methods, Geophys. J. Int. **167**, 70 (2006).

[7] P. Martin, Z. Aksamija, E. Pop, and U. Ravaioli, Impact of phonon-surface roughness scattering on thermal conductivity of thin Si nanowires, Phys. Rev. Lett. **102**, 125503 (2009).

[8] A. A. Maznev, Boundary scattering of phonons: Specularity of a randomly rough surface in the small-perturbation limit, Phys. Rev. B **91**, 134306 (2015).

[9] F. Shi, M. Lowe, and R. Craster, Diffusely scattered and transmitted elastic waves by random rough solid-solid interfaces using an elastodynamic Kirchhoff approximation, Phys. Rev. B **95**, 214305 (2017).

[10] N. K. Ravichandran, H. Zhang, and A. J. Minnich, Spectrally resolved specular reflections of thermal phonons from atomically rough surfaces, Phys. Rev. X **8**, 041004 (2018).

[11] D. Gelda, M. G. Ghossoub, K. Valavala, J. Ma, M. C. Rajagopal, and S. Sinha, Specularity of longitudinal acoustic phonons at rough surfaces, Phys. Rev. B **97**, 045429 (2018).

[12] F. Shi, Variance of elastic wave scattering from randomly rough surfaces, J. Mech. Phys. Solids **155**, 104550 (2021).

[13] J. Lim, K. Hippalgaonkar, S. C Andrews, A. Majumdar, and P. Yang, Quantifying surface roughness effects on phonon transport in silicon nanowires, Nano Lett. **12**, 2475 (2012).

[14] J. A. Ogilvy, Wave scattering from rough surfaces, Rep. Prog. Phys. **50**, 1553 (1987).

[15] J. A. DeSanto, *Scalar Wave Theory* (Springer, Berlin, 1992).

[16] Z. Aksamija and I. Knezevic, Lattice thermal conductivity of graphene nanoribbons: Anisotropy and edge roughness scattering, Appl. Phys. Lett. **98**, 141919 (2011).

[17] G. A. Northrop and J. P. Wolfe, Phonon reflection imaging: A determination of specular versus diffuse boundary scattering, Phys. Rev. Lett. **52**, 2156 (1984).

[18] C. Shao, Q. Rong, M. Hu, and H. Bao, Probing phonon-surface interaction by wave-packet simulation: Effect of roughness and morphology, J. Appl. Phys. **122**, 155104 (2017).

[19] J. B. Hertzberg, M. Aksit, O. O. Otelaja, D. A. Stewart, and R. D. Robinson, Direct measurements of surface scattering in Si nanosheets using a microscale phonon spectrometer: Implications for casimir-limit predicted by ziman theory, Nano Lett. **14**, 403 (2014).

[20] N. Mingo and L. Yang, Phonon transport in nanowires coated with an amorphous material: An atomistic Green's function approach, Phys. Rev. B **68**, 245406 (2003).

[21] Z.-Y. Ong, Tutorial: Concepts and numerical techniques for modeling individual phonon transmission at interfaces, J. Appl. Phys **124**, 151101 (2018).

[22] Z.-Y. Ong, Atomistic *S*-matrix method for numerical simulation of phonon reflection, transmission, and boundary scattering, Phys. Rev. B **98**, 195301 (2018).

[23] C. K. Gan and Z.-Y. Ong, Complementary local-global approach for phonon mode connectivities, J. Phys. Commun. **5**, 015010 (2021).

[24] C. Shao, Q. Rong, N. Li, and H. Bao, Understanding the mechanism of diffuse phonon scattering at disordered surfaces by atomistic wave-packet investigation, Phys. Rev. B **98**, 155418 (2018).

[25] Y. Kuang, L. Lindsay, S. Shi, X. Wang, and B. Huang, Thermal conductivity of graphene mediated by strain and size, Int. J. Heat Mass Transf. **101**, 772 (2016).

[26] J. D. Gale and A. L. Rohl, The general utility lattice program (GULP), Mol. Simul. **29**, 291 (2003).

[27] D. W. Brenner, O. A. Shenderova, J. A. Harrison, S. J. Stuart, B. Ni, and S. B. Sinnott, A second-generation reactive empirical bond order (REBO) potential energy expression for hydrocarbons, J. Phys.: Condens. Matter **14**, 783 (2002).

[28] L. Lindsay and D. A. Broido, Optimized Tersoff and Brenner empirical potential parameters for lattice dynamics and phonon thermal transport in carbon nanotubes and graphene, Phys. Rev. B **81**, 205441 (2010).

[29] Z.-Y. Ong and G. Zhang, Efficient approach for modeling phonon transmission probability in nanoscale interfacial thermal transport, Phys. Rev. B **91**, 174302 (2015).

[30] L. Yang, B. Latour, and A. J. Minnich, Phonon transmission at crystalline-amorphous interfaces studied using mode-resolved atomistic Green's functions, Phys. Rev. B **97**, 205306 (2018).

[31] Z.-Y. Ong, G. Schusteritsch, and C. J. Pickard, Structure-specific mode-resolved phonon coherence and specularity at graphene grain boundaries, Phys. Rev. B **101**, 195410 (2020).

[32] Z.-Y. Ong, Specular transmission and diffuse reflection in phonon scattering at grain boundary, Europhys. Lett. **133**, 66002 (2021).